行政院國家科學委員會補助專題研究計畫

☑ 成果報告
□期中進度報告

（計畫名稱）

過渡金屬氧化物薄膜物理與元件研究--超導與磁性鈣鈦礦氧化物薄膜之界面特性與混成結構研究(3/3)

計畫類別：□ 個別型計畫　☑ 整合型計畫
計畫編號：NSC 94－2112－M－009 －007－
執行期間：2005 年 08 月 01 日至　2006 年 08 月 31 日

計畫主持人：莊振益
共同主持人：
計畫參與人員：謝志昌、鄭瓈耀、李家宏、林宗漢、劉凱銘、李秉翰、陳右儒

成果報告類型(依經費核定清單規定繳交)：□精簡報告☑完整報告

本成果報告包括以下應繳交之附件：
□赴國外出差或研習心得報告一份
□赴大陸地區出差或研習心得報告一份
☑出席國際學術會議心得報告及發表之論文各一份
□國際合作研究計畫國外研究報告書一份

處理方式：除產學合作研究計畫、提升產業技術及人才培育研究計畫、列管計畫及下列情形者外，得立即公開查詢
□涉及專利或其他智慧財產權，□一年□二年後可公開查詢

執行單位：交通大學電子物理系

中　華　民　國　95　年　11　月　28　日

Content

Page

[中文摘要]

關鍵詞：多鐵、反鐵磁相轉變、摻雜比例、金屬絕緣相轉變、缺鑭錳氧化物

在多鐵材料 $YMNO_3$ 中摻雜不同離子半徑的鹼土族金屬，用固態燒結的方式製作一系列的樣品 $Y_{1-x}A_xMnO_3$ ($A = Ca, Sr ; x = 0, 0.1, 0.3, 0.5$)，探討 Y^{+3} 離子被不同元素與攙雜比例取代後的影響。比較 $Y_{1-x}Ca_xMnO_3$ ($x = 0, 0.1, 0.3, 0.5$)系列的樣品，我們發現隨著Ｃa^{+2} 摻雜比例”x”的增加，$Y_{1-x}Ca_xMnO_3$ 的晶體結構會由 hexagonal 轉變為 orthorhombic；相對地 $Y_{1-x}Sr_xMnO_3$ ($x = 0, 0.1, 0.3, 0.5$)系列的樣品呈現 hexagonal 的結構不會隨著 Sr 攙雜比例而有所改變。由磁化率對溫度的量測，鈣攙雜的樣品其反鐵磁相轉變溫度為（30.4K），相較於純 $YMnO_3$(42.5K)有往低溫（30.4K）移動的趨勢；另一方面，鍶摻雜的樣品其反鐵磁相轉變溫度只有些微地下降至 38K。反鐵磁行為的些微變化可以看作因摻雜不同離子張力造成的影響。比較 Mn^{+2}、Mn^{+3}、Mn^{+4} 標準樣品同步輻射的吸收光譜與我們樣品的差異性，$YMnO_3$ 與 $Y_{1-x}Sr_xMnO_3$ 展現了同於 Mn_2O_3 標準粉末的 Mn^{+3} 相似特徵。但鈣摻雜的 $YMnO_3$ 樣品與 $YMnO_3$ 本身有著極大的差異性。但是令人好奇的是鈣離子的離子半徑與釔離子相近，應該對晶格的改變會是最小的變化，但我們實際上觀察到的是，由於鈣摻雜在 $YMnO_3$ 的結構中，造成了結構的改變也影響了其磁特性與電子結構。

另一方面，我們已使用雷射蒸鍍法在鋁酸鑭基板上製備了單相的 $La_{0.7}Sn_{0.3}MnO_3$ (LSnMO)薄膜。直接成長的薄膜的特性為金屬性絕緣體，其居禮溫度約為 180K。從 x-ray absorption spectroscopy (XAS)的結果可證明摻雜錫的確使的 LSnMO 中的 Mn 成為 Mn^{3+}/Mn^{2+}的混和態。由 TEM 所得到的結果顯示：我們成功的在 LSnMO 系統中將錫的摻雜比例提升至 0.3。此外，我們研究了 LSnMO 在氧氣與氬氣環境下做熱處理的各種性質。從 XAS 與 TEM 的結果可證明，在氧氣環境下做熱處理的 LSnMO 樣品產生了錫的氧化物。所得到的磁性與傳輸的特性是來自於缺鑭錳氧化物(La-deficient $La_{1-x}MnO_3$ phases)所造成。

Abstract (in English)

Keywords: multiferroic、antiferromagnetic phase transition、doping levels、insulator-metal transition 、La-deficient $La_{1-x}MnO_3$ phases

A series of doped multiferroic samples $Y_{1-x}A_xMnO_3$ (A = Ca, Sr ; x = 0, 0.1, 0.3, 0.5) were prepared to investigate the effects of replacing Y^{3+}. We found that, for the $Y_{1-x}Ca_xMnO_3$ (x = 0, 0.1, 0.3, 0.5) series, the crystal structure evolved from hexagonal to orthorhombic structure with increasing x. For the Ca-doped samples, the antiferromagnetic (AFM) phase transition appears to take place at a much lower temperature (30.4 K) as compared to that of undoped one (42.5 K). On the other hand, when doped with larger Sr-ions, the AFM temperature decreased only slightly to 38 K. Nevertheless, the AFM transition was significantly smeared, indicating that strain may have come into play. By comparing the XANES results to the standard manganese oxide powders with valence of Mn^{+2}, Mn^{+3}, and Mn^{+4}, both $YMnO_3$ and $Y_{1-x}Sr_xMnO_3$ exhibit the dominant Mn^{+3} characteristics similar to that obtained from the standard Mn_2O_3 powder. It is surprising to observe that Ca-doping has resulted in most significant modifications in the magnetic property and electronic structure of $YMnO_3$, since Ca^{+2} is having exactly the same ionic size as that of Y^{+3} and is expected to cause minimal distortion on the lattice.

The single-phase $La_{0.7}Sn_{0.3}MnO_3$ (LSnMO) thin films were fabricated by pulsed laser deposition (PLD). The as-deposited films did display a paramagnetic-ferromagnetic transition (PFT) around 180 K. The x-ray absorption spectroscopy (XAS) of the as-deposited LSnMO films shows signature of Mn^{3+}/Mn^{2+} mixed-valence. The transmission electron microscopy (TEM) analyses on the as-deposited LSnMO films further confirmed that the films are epitaxial with uniform composition distributions. In the oxygen-annealing case, the evidence from the XAS measurements on Sn ions though showed the existence of tetravalent characteristics, the TEM analyses also revealed the emergence of the Sn-compounds, which may ultimately drive the obtained films into La-deficient $La_{1-x}MnO_3$ phases.

I. Anomalous ionic size effect in doped multiferroic $Y_{1-x}A_xMnO_3$(A=Ca, Sr)

1. Motivation

Multiferroic materials are novel materials which display the co-existence of various competing orderings, such as ferromagnetic, ferroelectric, antiferromagnetic, as well as the elastic orders [1-4]. The characteristics of multiferroics not only promise the potential applications in magneto-electrical devices (in that the magnetic ordering can be manipulated by applying an electric field and vice versa [2-4]), but also pose exciting challenges in understanding the underlying fundamental physics. Traditional ferroelectric materials like $BaTiO_3$ with ABO_3 perovskite structure requires empty d-orbital and full electrons in p-orbital [1,5]. On the contrary, the general ferromagnetism needs localized B-site d-orbital electrons [6-7]. Owing to the chemical incompatibility, only a few materials have been found to simultaneously possess both magnetic and ferroelectric characteristics, and were termed as "multiferroics" [1]. The materials exhibiting the multiferroic characteristics can be cataloged into several classifications, namely, (i) the Bi-based compound like $BiFeO_3$ or $BiMnO_3$ [1]; (ii) the $ReMnO_3$ perovskites (Re = Tb、Dy、Y、Ho、Er、Tm、Yb、Lu) [1-3, 8-14]; and (iii) the $ReMn_2O_5$ double perovskites (Re = Y、Tb、Dy、Ho) [1,4]. Interestingly, many of the $ReMnO_3$ perovskites are also representative materials showing the colossal magnetoresistance (CMR) [6-7].

It has been established that, in this family, the decreasing ionic size of the rare earth elements gradually drives the structure of $ReMnO_3$ from orthorhombic into hexagonal and only the hexagonal manganese oxides have the ferroelectric properties. Y^{+3} (1.06Å) has the critical ionic size for the variation of structure, and, as a result, $YMnO_3$ can have both orthorhombic and hexagonal phase. The ferroelectric polarization along the c-axis in $YMnO_3$ comes from the structure distortion such as tilted MnO_5 and displacement of Y^{+3} ions [8]. It is, thus, interesting to conduct a systematic study to see how the lattice distortion induced by ion size difference affects the physical properties of this material. In this paper, we report the magnetic properties, O K-edge X-ray absorption near edge spectroscopy (XANES) and Mn L edge XANES on a series of doped multiferroic materials $Y_{1-x}A_xMnO_3$ (A = Ca, Sr ; x = 0, 0.1, 0.3, 0.5) obtained by the solid-state reactions and discuss how the doped ionic size and doping level affect the magnetic properties and electronic structure of this material.

2. Experiment

All the samples of $Y_{1-x}A_xMnO_3$ (A = Ca, Sr ; x = 0, 0.1, 0.3, 0.5) were prepared by solid state reaction from adequate quantities of Y_2O_3(99.999%), $MnCO_3$(99.95%), $CaCO_3$(99.95%) and $SrCO_3$(99.99%). Y_2O_3 was preheated to 500℃ for 5h to remove the adsorbed mist. The desired mixture of Y_2O_3, $MnCO_3$, $CaCO_3$, and $SrCO_3$ were then heated at 1300℃ for 12h. It was ground to mix again and heated to 1300℃ for 24h. The resultant powder was then pressed into cylinders and reheated to 1300℃ for 36h. We compared the density of these bulks with that calculated from the ideal unit cell parameters and repeated the grind-press-reheat processes until the density approaching that of ideal bulks. The crystalline structure, magnetization behaviors, and electronic structure of these samples were examined by x-ray diffraction (XRD), Superconducting Quantum Interference Device (SQUID), and x-ray absorption near edge spectroscopy (XANES), respectively. The XANES spectra were collected by the total electron yield (TEY) mode.

3. Results and discussion

From the XRD θ-2θscans presented in Fig. 1, it is clear that the undoped $YMnO_3$ is of pure hexagonal structure. The Sr^{2+}-doped $YMnO_3$ also shows hexagonal structure for various doping levels, as well. On the other hand, the structure of the $Y_{1-x}Ca_xMnO_3$ samples varies from the hexagonal structure for undoped $YMnO_3$ and to hexagonal-orthorhombic mixed for $Y_{0.9}Ca_{0.1}MnO_3$. When x = 0.3, the character of hexagonal structure becomes diminishingly insignificant and completely disappears when x = 0.5. By comparing the main peak around 2θ = 33.17° (hexagonal $YMnO_3$(112)), an angle shift of 0.04°, .033°, and 0.51° was observed for x = 0.1, 0.3, and 0.5, respectively. This is quite surprising if one looks at the ionic size of Y^{+3}, Ca^{+2}, and Sr^{+2}, which are 1.06Å, 1.06 Å, and 1.27 Å, respectively. Intuitively, the fact that Ca^{+2} having nearly the same ionic size as Y^{+3} should result in a much smaller distortion on the crystal structure than Sr^{2+} will do when substitution is taking place. We note that similar results were reported by Agüero et al. in their study on $Y_xCa_{1-x}MnO_3$ (0.1<x<1) [15] and had been explained by that the differences in the Mn electronic state might overcome the differences in ionic size.

In order to check if the modification of the electronic state of Mn-ion by substituting Y with Ca and Sr is indeed relevant to the changes in crystal structure, we have performed extensive XANES measurements on all the samples. The Mn L edge XANES of $YMnO_3$, $Y_{0.9}Ca_{0.1}MnO_3$, and $Y_{0.9}Sr_{0.1}MnO_3$ are shown in Fig. 2, together with that obtained from standard manganese oxide powders with valence of Mn^{+2} (MnO), Mn^{+3} (Mn_2O_3), and Mn^{+4} (MnO_2). This practice has been widely used to characterize the light hole-doped $YMnO_3$ polycrystalline samples [10] as well as various manganites [7, 9]. As is evident from the results, the electronic structure all $Y_xCa_{1-x}MnO_3$ samples exhibit characteristics very similar to that of the Mn_2O_3 standard powders, indicating that Mn ions are predominantly trivalent. The doping of Ca and Sr does not noticeably displace the +3 valence states of $3d^4$ configuration. The minor difference appeared in the range of 642.5~645eV, though may be suggestive for the signature of existing Mn^{+4} character (by comparing with the spectrum of the standard MnO_2 powders, is attributed to the chemical shift caused by changes in electrostatic energy at the Mn site driven by balancing Y^{+3} replacements in the ionic valance. In any case, no signature was observed for indication of divalent manganese in all samples.

Fig. 3 shows the O K edge total electron yield XANES for the three samples discussed in Fig. 2. The peaks appeared in the spectra were consisted of four groups (A, B, C, D). The first 3 peaks (A_1 = 530eV, A_2 = 531.2eV, A_3 = 532.6eV) were assigned as group A, followed by 2 group B peaks (B_1 = 534.1eV, B_2 = 535.8eV). Group C consists of only a peak centered at 538.2eV, and the final 2 peaks (D_1 = 541.2eV, D_2 = 542.6eV) are referred to group D. These groups are associated with transitions between O 2p-Mn 3d states (group A and B), O 2p-Y 3d states (group C), and O 2p-Mn 4sp hybridization (group D) around 530~535, 538, and 543eV, respectively. Microscopically, for the manganese ions residing in the triangular MnO_5 bi-pyramid, the O 2p-Mn 3d orbital split into 3 components (e_1, e_2, and a_1) induced by the crystal field. The e_1, e_2, and a_1 are associated with the states $3d_{xz,yz}$ (A_1, A_2), $3d_{xy,\, x^2-y^2}$ (A_3, B_1) and $3d_{3z^2-r^2}$(B_2) in the order of increasing energy, respectively [9-11]. Due to the modified distortion in MnO_5, there exist differences between the electronic structures of orthorhombic and hexagonal $ReMnO_3$ (Re: rare earth). The observation of the fine and distinguishable peaks A_1, A_2, A_3, B_1, and

B_2 being merged into two broad ones (A and B) has been a manifestation of the hexagonal to orthorhombic structure change. For instance, $Y_{0.9}Ca_{0.1}MnO_3$ showed both hexagonal and orthorhombic features in the XRD scan, resulting in a significant spectral weight transferring between the A_3 and B_2 peaks which appeared as merging peaks B_1, B_2, and C into one broad peak. In contrast, the XANES of $YMnO_3$ and $Y_{0.9}Sr_{0.1}MnO_3$ showed similar features, which is consistent with the fact that both samples are remaining hexagonal. The current results further suggest that the electronic structure may have played a more important role than the ionic size effect in determining the crystal structure as has been argued by Agüero et al. [15]. The underlying mechanism for this peculiar behavior and the corresponding effect on ferroelectricity, however, requires further studies.

Finally, we present the preliminary magnetic properties of the polycrystalline $Y_{1-x}A_xMnO_3$ samples by showing the temperature dependent magnetization in Fig. 4. For Sr-doped samples, $Y_{0.9}Sr_{0.1}MnO_3$ and $Y_{0.7}Sr_{0.3}MnO_3$, the antiferromagnetic (AFM) transition temperature is around 38.4 K, slightly lower than 42 K of the undoped $YMnO_3$. The AFM transition becomes undetectable for both $Y_{0.5}Sr_{0.5}MnO_3$ and $Y_{0.5}Ca_{0.5}MnO_3$. On the other hand, although the AFM transition temperature for $Y_{0.9}Ca_{0.1}MnO_3$ and $Y_{0.7}Ca_{0.3}MnO_3$ has been further reduced to 34 K, the magnetization signal has been dramatically improved by about 30 times with Ca^{+2} doping. The suppressed Néel temperature has been attributed to the strong spin frustration in the triangular lattice of Mn^{3+} ions and weak interplane exchange interaction specific to the hexagonal structure of $ReMnO_3$ [9, 11]. It will be interesting to figure out what's happened as the crystal structure being driven into orthorhombic by Ca-doping.

4. Summary

In summary, we have prepared a series of $Y_{1-x}A_xMnO_3$ (A = Ca, Sr ; x = 0, 0.1, 0.3, 0.5) samples to systematically investigate the interplays between the crystal structure, magnetic properties, and the electronic structures revealed by XANES measurements. The results indicate that Ca-doping drives the hexagonal $YMnO_3$ into orthorhombic structure. The XANES spectra showed that the spectral weight transferring might have also occurred with Ca–doping, and is consistent with the accompanied structural changes. On the other hand, Sr-doping seemed to have very little effects on various properties of $YMnO_3$. The observations are somewhat counter-intuition and thus intriguing, since Sr^{2+} is having larger ionic size difference than Ca^{2+} as compared to Y^{3+} ions. Further studies are certainly needed for clarifying these issues.

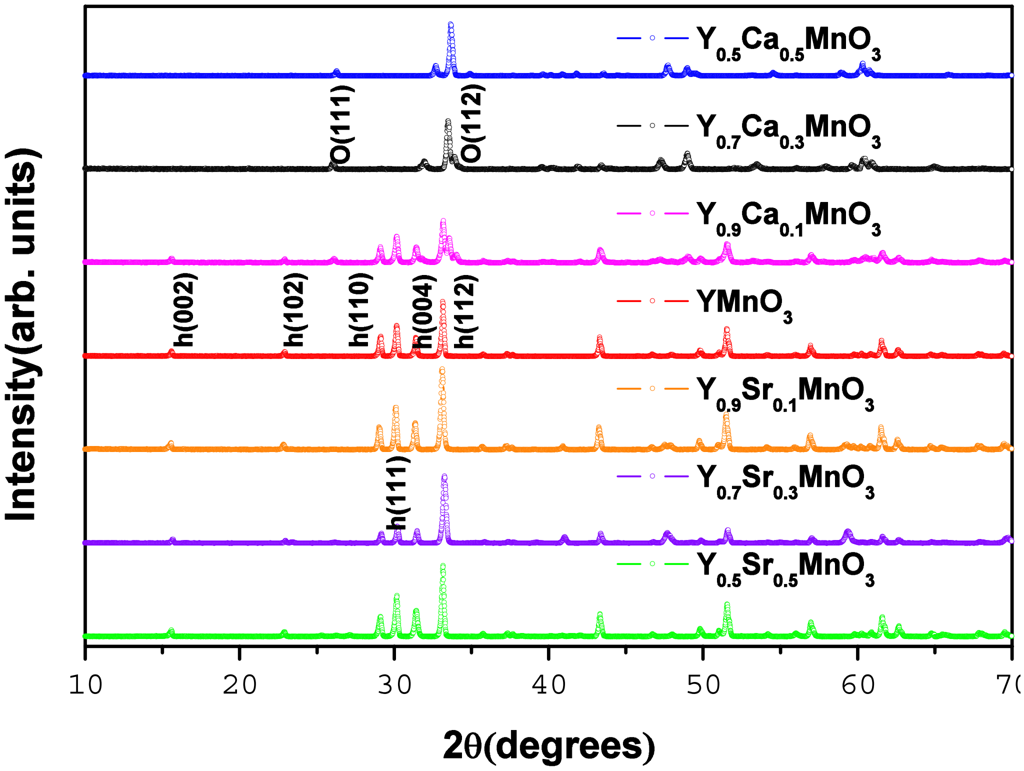

FIG. 1: The XRD patterns for a series $YMnO_3$ doped with Ca and Sr. Both pristine $YMnO_3$ and $Y_{1-x}Sr_xMnO_3$ samples show the same hexagonal crystal structure. The structure of $Y_{1-x}Ca_xMnO_3$ changes from hexagonal to orthorhombic with the increasing doping level of Ca^{+2}.

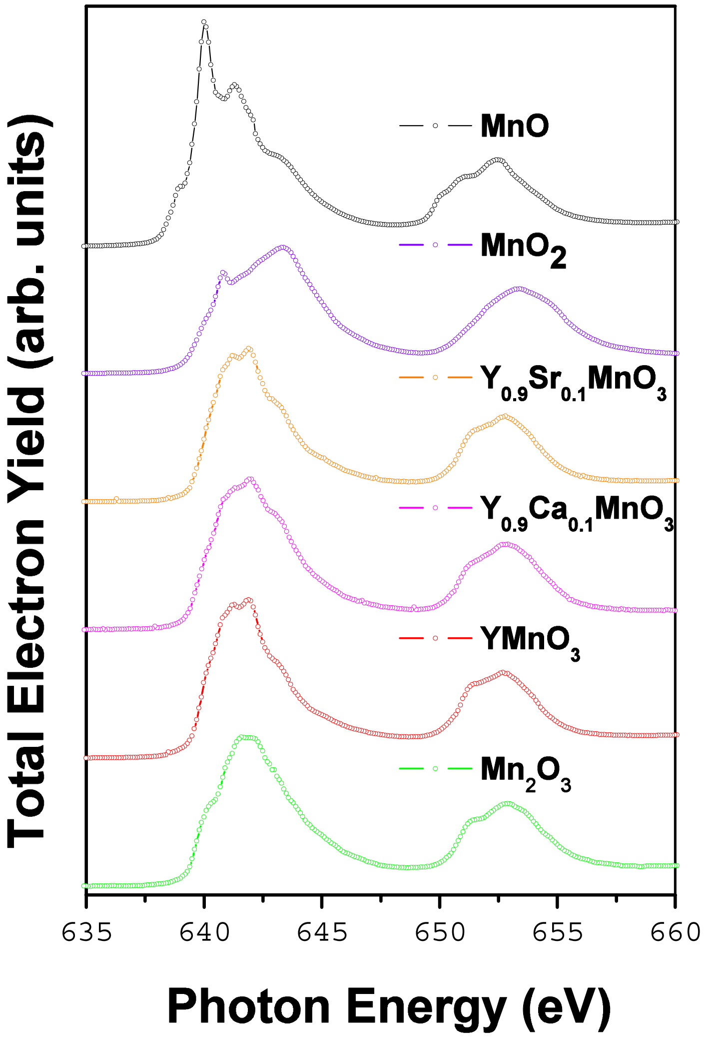

FIG. 2: The Mn L edge XANES spectra for MnO (standard powder), MnO_2 (standard powder), $Y_{0.9}Sr_{0.1}MnO_3$, $Y_{0.9}Ca_{0.1}MnO_3$, $YMnO_3$, and Mn_2O_3 (standard powder). Data presented in order from top to bottom.

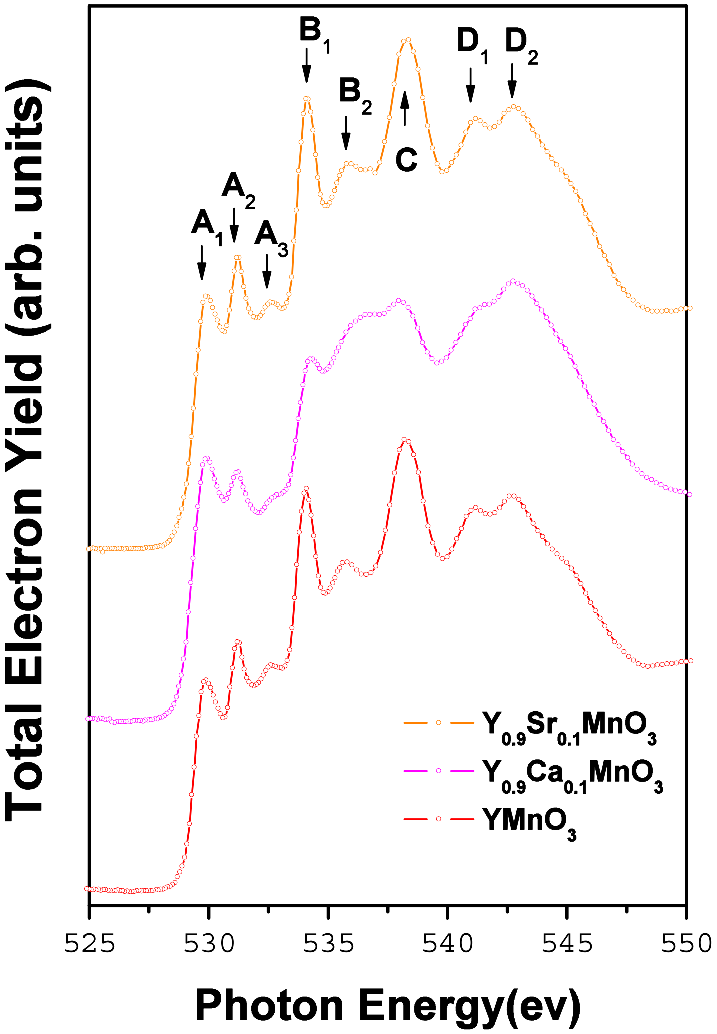

FIG. 3: The O K edge XANES spectra in order of $Y_{0.9}Sr_{0.1}MnO_3$, $Y_{0.9}Ca_{0.1}MnO_3$, and $YMnO_3$ from top to bottom.

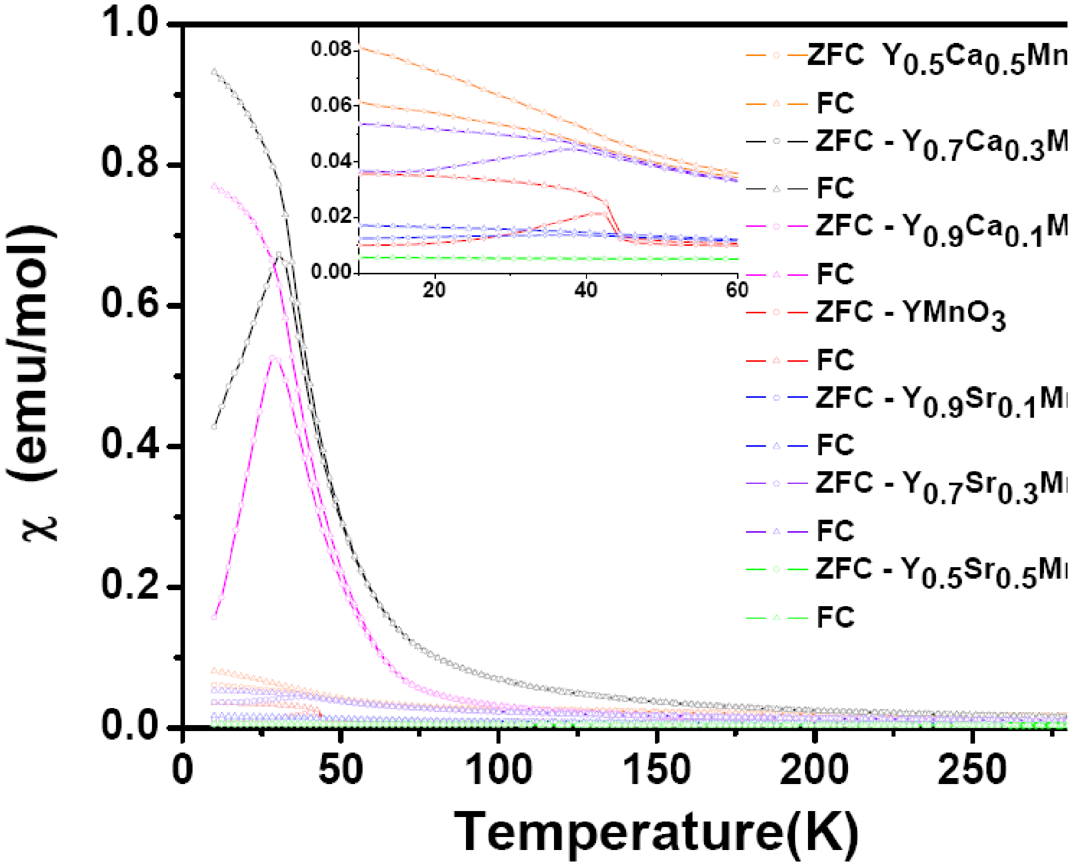

FIG. 4: Temperature dependence of magnetization for all $Y_{1-x}A_xMnO_3$ (A = Ca, Sr ; x = 0.1, 0.3, 0.5) polycrystalline samples measured by zero field cooled (ZFC) scheme with an applied field of 100 Oe.

References

[1] W. Prellier, M.P. Singh, and P. Murugavel, J. Phys.: Condens. Matter 17, 803 (2005).

[2] M. Fiebig, Th. Lottermoser, D. Fro¨ hlich, A. V. Goltsev, and R. V. Pisarev, Nature 419, 818 (2002).

[3] T. Lottermoser, T. Lonkai, U. Amann, D. Hohlwein, J. Ihringer, and M. Fiebig, Nature 430, 541 (2002).

[4] N. Hur, S. Park, P. A. Sharma, J. S. Ahn, G. Guha, and S-W Cheong, Nature 429, 392 (2004).

[5] N. A. Hill, J. Phys. Chem. B 104, 6694 (2000).

[6] W. J. Chang, C. C. Hsieh, J. Y. Juang, K. H. Wu, T. M. Uen, and Y. S. Gou, C. H. Hsu, J.-Y. Lin, J. Appl. Phys. 96, 4357 (2004).

[7] W. J. Chang, J. Y. Tsai, H.-T. Jeng, J.-Y. Lin, Kenneth Y.-J. Zhang, H. L. Liu, J. M. Lee, J. M. Chen, K. H. Wu, T. M. Uen, Y. S. Gou, and J. Y. Juang, Phys. Rev. B 72, 132410 (2005).

[8] B. B. Van Aken, T. T. M. Palstra, A. Filppetti, and N. A. Spaldin, Nature Mater. 3, 164 (2004).

[9] J.-S. Kang, S. W. Han, J.-G. Park, S. C. Wi, S. S. Lee, G. Kim, H. J. Song, H. J. Shin, W. Jo, and B. I. Min, Phys. Rev. B, 71, 092405 (2005).

[10] K. Asokan, C.L. Dong, C.W. Bao, H.M. Tsai, J.W. Chiou, C.L. Chang, W.F. Pong, P. Duran, C. Moure, O. Peña, Solid State Comm. 134, 821 (2005).

[11] A. B. Souchkov, J. R. Simpson, M. Quijada, H. Ishibashi, N. Hur, J. S. Ahn, S.W. Cheong, A. J. Millis, and H. D. Drew, Phys. Rev. Lett. 91, 027203-1, (2003).

[12] T. Katsufuji, S. Mori, M. Masaki, Y. Moritomo, N. Yamamoto, and H. Takagi, Phys.

Rev. B64, 104419 (2001).

[13] J.-S. Zhou, J. B. Goodenough, J. M. Gallardo-Amores, E. Morán, M. A. Alario-Franco, and R. Caudillo, Phys. Rev. B74, 014422 (2006).

[14] T. Katsufuji, M. Masaki, A. Machida, M. Moritomo, K. Kato, E. Nishibori, M. Takata, M. Sakata, K. Ohoyama, K. Kitazawa, and H. Takagi, Phys. Rev. B66, 134434 (2002).

[15] O. Agüero, A.G. Leyva, P. König, D. Vega, G. Polla, H. Aliaga, and M.T. Causa, Physica B 320, 47 (2002).

II. Magnetotransport properties, electronic structure, and microstructure of $La_{0.7}Sn_{0.3}MnO_3$ thin films

1. Motivation

The perovskite manganites, being a representative family of strong-correlated electron system, have been subject of extensive researches [1-2]. In particular, in various hole-doped manganites, the colossal magnetoresistance (CMR) effect, manifested by a paramagnetic-ferromagnetic transition at the Curie temperature (T_c) accompanied by a dramatic decrease in resistivity around a similar temperature (T_{IM}), has been ubiquitously observed and attributed to the charge-spin interaction of mixed-valence Mn^{3+}/ Mn^{4+} ions via Zener's seminal double-exchange (DE) mechanism [3]. However, it has been pointed out that DE alone might be inadequate to explain the observed CMR effect in $La_{1-x}Sr_xMnO_3$ and the incorporation of polaron effect induced by electron-phonon interactions arising from the Jahn-Teller splitting of the Mn d-levels could be essential [4]. On the other hand, despite the extensive success in obtaining the hole-doped manganites over wide range of compositions, efforts in trying to substitute La-ion with tetravalent ions and hence make the manganites electron-doped have been rather inconclusive. Joseph Joly *et al.* [5] argued that, due to the ion size constraints, it is almost impossible to replace the trivalent La^{3+} ion by tetravalent ions in polycrystalline manganite bulks prepared by solid state reaction. Indeed, early attempts of preparing Ce-doped $RMnO_3$ (*R*

＝La, Pr, Nd) manganites by Das and Mandal [6] all showed signatures of mixed-phases and hence blurred the interpretation of the obtained results. In particular, the replacement of tetravalent ions to La^{3+} often led to the self-doped $La_{1-x}MnO_{3-\delta}$ with localized multiphase compounds, which might give rise to very similar magneto-transport properties to those of the hole-doped manganites and jeopardize the genuine electron-doped characteristics [7, 8].

Recently, single-phase tetravalent-ion-doped $La_{0.7}Ce_{0.3}MnO_3$ (LCeMO) thin films were successfully fabricated by pulsed laser deposition (PLD) [9-12]. It appeared that ionic constraints and stoichiometry conservation could be compromised provided proper growth conditions were chosen. On the other hand, Kawai *et al.* [13] showed that, in their preparation scheme, while the as-grown LCeMO films all displayed ferromagnetic-insulator behavior, the typical metal-insulator transition are recovered only after post annealed under the atmosphere of oxygen and/or argon. The existence of the nano-clustering cerium oxides within the films revealed by TEM analyses has led the authors to conclude that cation deficiencies are responsible for the emergence of the ferromagnetic-metal characteristics, albeit the phase regions identified appeared to be rather minor. On the other hand, Zhang *et al.* [14] reported that the XPS of the $La_{0.9}Te_{0.1}MnO_3$ prepared by PLD and followed by annealing in the flowing oxygen revealed the signature of 4+ valence states for Te ions. They regarded it as the evidence of electron-doping for the $La_{0.9}Te_{0.1}MnO_3$ films. In addition, post annealed under the Ar environment was regarded as a possible method to fabricate the electron doped manganites. It is believed that the excess oxygen induces the holes carriers, which will compensate the electrons and increase the resistivity and probably weaken the double exchange interaction between Mn ions. Chen *et al.* [15] reported that the as-prepared $La_{1-x}Pr_xMnO_3$ (LPMO) bulks with different compositions do not show discernable metal-insulator transition behavior. However, the metal-insulator transition and associated CMR effect were obtained after annealing the samples in argon flow atmosphere. The XPS results of the Pr ions in their samples featured the characteristics of Pr^{3+} and Pr^{4+} mixture, indicating that the LPMO ceramic might be an electron-doped CMR compound. Compare to the potentially electron-doped CMR materials mentioned above, obtaining single-phase $La_xSn_{1-x}MnO_3$ (LSnMO) represents an even more severe challenge because of an even larger ionic size difference between La^{3+} and Sn^{4+}. Nevertheless, CMR effect has been observed in LSnMO [16-18], albeit the single-phase samples were hardly obtainable by the solid-state reaction technique and only limited doping (x = 0.1-0.2) has been achieved in thin film form. Since most manganites display optimum CMR effects around 30% doping and the prominent roles played by lattice degree of freedom in giving rise to both CMR [19] effect and phase-coexistence [20] phenomena, it is desirable to perform systematic studies on the LSnMO system with higher doping. In addition to the experimental facts briefly described above, there are some points noteworthy of mentioning. First, all attempts to substitute the tetra-valence ion (Ce, Sn, Te, Pr) into the La ion site frequently result in ferromagnetic-insulator CMR, suggesting either the lack of itinerant carriers or the exchange mechanism may be fundamentally different in the electron-doped regime. Second, post annealing under oxygen or argon environment has been a usual practice in fabricating the electron-doped manganites. However, samples prepared under these two annealing schemes can display markedly different transport and magnetic behaviors. Finally, it is not clear that the electronic states of the doped ions indeed directly reflect the doping states of the CMR materials. In this article, we present results obtained from the magneto-transport, electronic and microstructure analyses of the $La_{0.7}Sn_{0.3}MnO_3$ (LSnMO) that evidently clarify some of the outstanding issues mentioned above.

2. Experiment

Sintered LSnMO target was prepared by conventional solid-state reaction technique. LSnMO films were deposited on single crystalline $LaAlO_3$(100) substrates using a 248 nm KrF excimer laser operating at energy density of 2-3 J/cm^2. The details of the processing conditions can be found elsewhere [21]. The as-deposited films, though displayed usual paramagnetic-ferromagnetic transitions, the typical CMR behaviors of the accompanying insulator-metal transition was, however, absent. Thus, in some cases, subsequent *ex-situ* annealing was carried out at 800°C for 4 hours in 250 Torr of oxygen or argon. The temperature dependences of magnetization (M(T)) and magneto-transport properties were measured using a Quantum Design® PPMS system with a maximum applied field strength of 8 Tesla. The crystalline structure of the films was examined by x-ray diffraction (XRD) (θ-2θ scan) and x-ray scattering measurements. For the electronic structure and valence state of Mn and Sn ions, the x-ray absorption near edge spectroscopy (XANES) experiments were performed at the National Synchrotron Radiation Research Center of Taiwan. In order to probe the microstructure, interface between film and substrate, as well as the element distributions of the LSnMO films, cross-section transmission electron microscopy (TEM) and electron energy loss spectroscopy (EELS) mapping were performed.

3. Results and discussion

3.1 Transport and magnetic behaviors

Fig. 3.1—3.3 shows the field-cooled and zero-field-cooled temperature-dependent magnetizations $M(T)$ measured at applied field of 0.1 T and 0.01 T together with the zero-field temperature dependence of resistivity $\rho(T)$ for Fig. 3.1 the as-deposited (AD) and Fig. 3.2 the oxygen-annealed (PA) LSnMO films as well as for Fig. 3.3 the argon-annealed (ArPA) LSnMO film measured at 0.1 T, respectively. We note that in the paramagnetic (PM) state the resistivity of the AD-film is larger than that of the PA-films by nearly two orders of magnitude. While this may originate from the charge localization effects associated with lattice distortion [22, 23], the absence of a temperature-induced T_{IM} in the AD-film can be more subtle and complicated. De Teresa *et al.* [24] argued that it might be related to the absence of long range FM order signified with a manifestation of spin-glass-like behavior at lower temperatures. This would imply that the large epitaxial strain originally existent in the AD-film not only induces enormous charge localization effect but also hinders the formation of long range FM ordering. If this argument is true, one expects to see the opposites for the PA-films. At the first glance, it seems to explain the over 200% enhancement in magnetization and dramatic increase in T_{IM} rather consistently. However, as shown in Fig. 3.1—3.3, significant spin-glass-like behavior, characterized by the pronounced irreversibility between the field-cooled (FC) and zero-field-cooled (ZFC) M(T) curves, is evident for both cases. This implies that the insulator-metal transition and spin-glass state are not necessary mutually exclusive.

Furthermore, we note that the results shown in Fig. 3.1－3.3 also reveal some features deviating from that reported for low-doping LSnMO [18]. In that progressive suppression of spin-glass-like behavior with increasing Sn-doping was observed. It has been interpreted as a result of increasing Mn^{4+} ions driven by Sn-doping-induced La-vacancies, and the low-doping LSnMO's were essentially regarded as hole-doped manganites. However, according to the XAS results to be presented below, the features of Mn^{2+}/Mn^{3+} mixed-valences indicate that the present AD-films might have effectively doped some electrons to the e_g-band of Mn-3d orbitals. Furthermore, we note that, in our case (x ＝ 0.3) the spin-glass-like transition not only emerges at much higher temperature ($T_g \approx 150$ K) than that reported in Ref. 14 (75 K → 20 K for x ＝ 0.04→ 0.18) but also is very sensitive to the applied field. Thus, we suspect that the Sn-doping-induced La-vacancies scenario may not apply to our case. The spin-glass-like behavior and CMR effect observed in the annealed LSnMO here is probably not arising from the divalent doping-enhanced ferromagnetic interaction and magnetic homogeneity but maybe related to the strain relaxation in a subtler manner. The other feature to be noted is the dramatic suppression of the low temperature magnetization for the AD-film when measured at 0.01 T. Since the basic ingredients for spin-glass to occur are disorder as well as the magnetic interaction randomness, anisotropy and frustrations[19], we believe that these factors also account for the dramatic suppression of magnetization in the lower measuring fields for the AD-films. Finally, we note that very recent observations by Valencia *et al*. [25] have indicated that, in $La_{2/3}Ca_{1/3}MnO_3$ films, the formation of Mn^{2+} ions due to the instability of Mn^{3+} subjected to prolonged air exposure might also lead to charge localization and, hence, the increasing resistivity and reducing magnetization. However, the relevance of this non-ferromagnetic order originated from divalent Mn component to the observed spin-glass-like behaviors discussed above remains to be clarified.

On the other hand, since post annealing by argon is a common practice for preparing the tetravalent-doped CMR materials, it is important to clarify the effect of argon annealing on LSnMO films. The idea behind this practice was that the excessive oxygen may induce hole doping, and thus, may counteract the expected effect of electron-doped CMR materials. Therefore, annealing in the argon environment may avoid the introduction of holes induced by excess oxygen and could turn out to be a practical method of fabricating electron-doped CMR materials. As illustrated in Fig. 3.3, the M-T of the argon-annealed LSnMO (ArPA LSnMO) film does display a comparable magnetization to that of the PA-LSnMO film. Nonetheless, the zero-field temperature dependent resistivity, ρ(T), is about three times larger than that of the PA-LSnMO film. Since, in contrast to the AD films, both PA- and ArPA-LSnMO films exhibit signatures of typical paramagnetic-insulator (PI) to ferromagnetic-metal (FM) transition, annealing appears to have effects on driving the material from a ferromagnetic insulator to a ferromagnetic metal. However, there exist some differences in the detailed behaviors between the PA- and ArPA-films, as well.

Fig. 3.4－3.5 shows ρ(T) as a function of applied field for the PA film and ArPA film, respectively. The resistivity was measured with the field applied parallel to the film surface. For the AD-film, although there exists a typical PM-FM transition with $T_c \approx 190$ K, the ρ(T) increases steeply with decreasing temperature (Fig. 3.1) and has no sign of metallic transition for applied field up to 8 Tesla. On the contrary, for the PA-film, in addition to having a nearly two orders of magnitude reduction in resistivity as compared to the AD-film in the PM state, it also displays the typical CMR behavior with $T_{IM} \sim 300$ K at zero-field. The maximum magnetoresistance (MR) ratio, defined as $\Delta\rho/\rho = (\rho(0)-\rho(H))/\rho(0)$ with $\rho(0)$ and $\rho(H)$ being the resistivity at zero field and at field H, appears around 250 K and reaches about 70% at a field of 8 Tesla. Together with the *M*(T) results shown in Fig. 3.1—3.3, the results demonstrate that annealing not only significantly enhances the low-temperature magnetization by more than 200% but also changes the magneto-transport properties of the LSnMO films dramatically. Guo *et al.*[17], by varying the film thickness in their $La_{0.9}Sn_{0.1}MnO_{3+\delta}$ films, have found similar enhancement in raising T_{IM} with increasing film thickness. However, there was no noticeable change in T_c and low temperature magnetization with film thickness variations, which led them to conclude that the enhancement of T_{IM} was due to strain relaxation instead of formation of new phases introduced by oxygen- or La-deficiency [7-8, 20, 25-28]. Similarly, Thomas *et al.* [29] have attributed the improved magneto-transport properties observed in their high temperature (900°C) annealed $La_{0.7}Ca_{0.3}MnO_3$ films to the massive stress relaxation and improved film crystallinity accompanied with grain growth. However, they did not report how magnetization and T_c were affected by post-annealing. In comparison, for the ArPA-films, although it also displays the typical CMR behavior, the $T_{IM} = 230$ K at zero-field is somewhat lower than that of the PA films. The maximum MR ratio appears around 220 K and reaches nearly about 95% at a field of 8 Tesla. These results are, in fact, very similar to that of some La-deficient CMR materials [20, 24]. It appears that, from the magneto-transport properties alone, one cannot discern whether the typical CMR behaviors displayed by post-annealed films are indeed the genuine characteristics of electron-doped manganites or they are just manifestations of La-deficient manganites induced by post annealing [11]. In addition, whether the lack of insulating-metallic transition in AD-LSnMO films is correlated to the lattice disorder or to other mechanisms (such as composition change) remains to be clarified. In order to give some further accounts on these issues, we performed further investigations on the electronic structures of the corresponding films by XAS measurements.

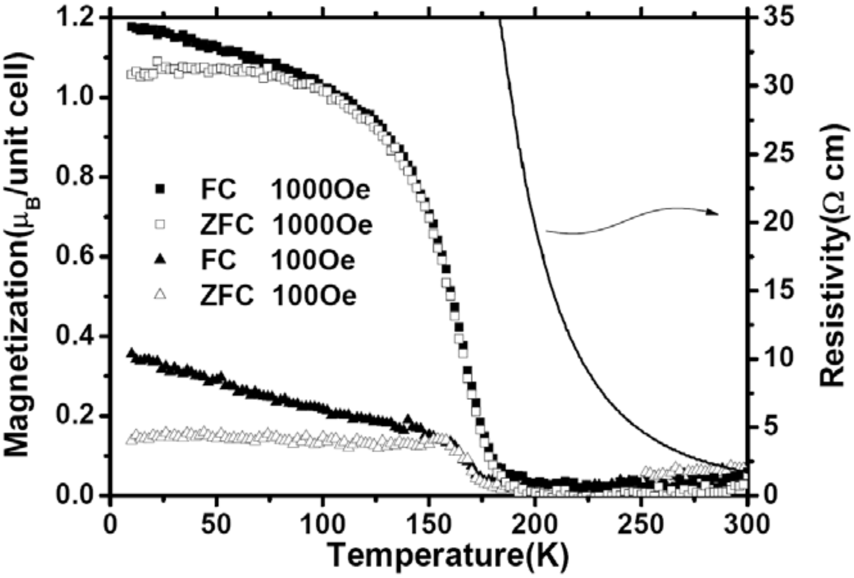

Figure 3.1: The field-cooled and zero-field-cooled temperature-dependent magnetizations (M(T)) measured at 0.1 T and 0.01 T for the as-deposited (AD) LSnMO film.

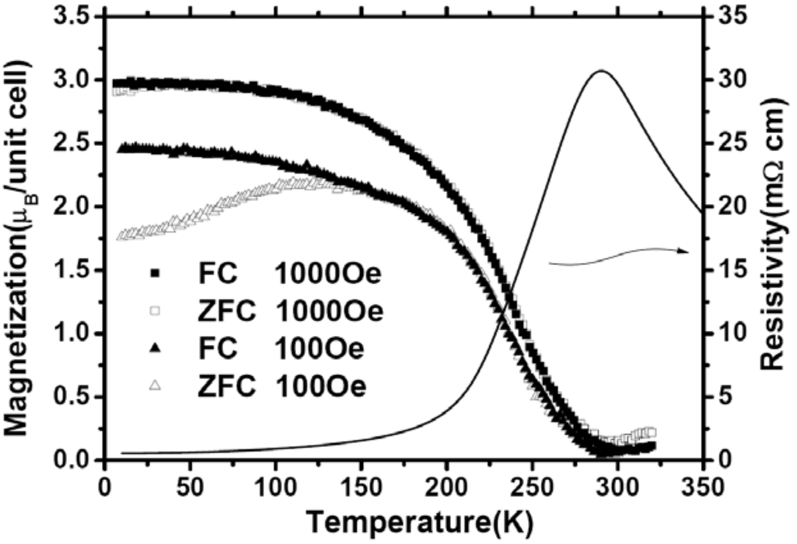

Figure 3.2: The field-cooled and zero-field-cooled temperature-dependent magnetizations (M(T)) measured at 0.1 T and 0.01 T for the oxygen-annealed (PA) LSnMO film.

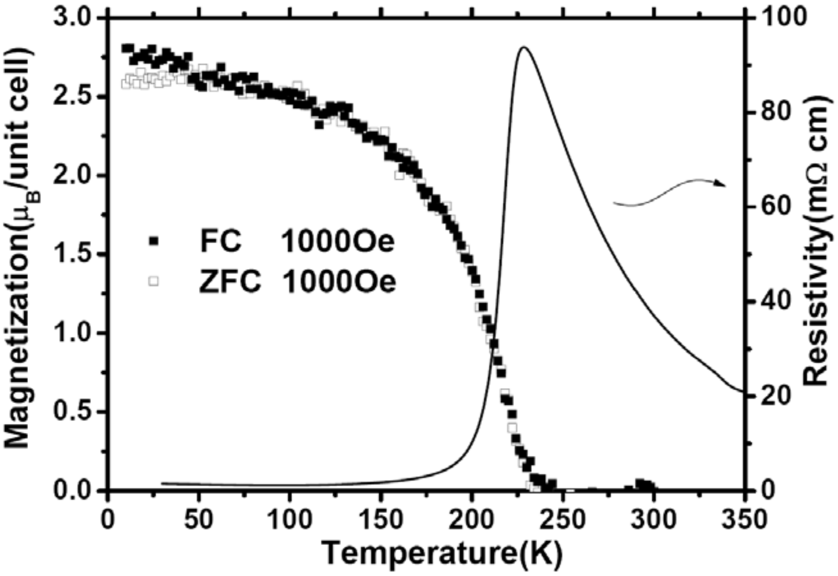

Figure 3.3: The field-cooled and zero-field-cooled temperature-dependent magnetizations (M(T)) measured at 0.1 T for the argon-annealed (ArPA) LSnMO film.

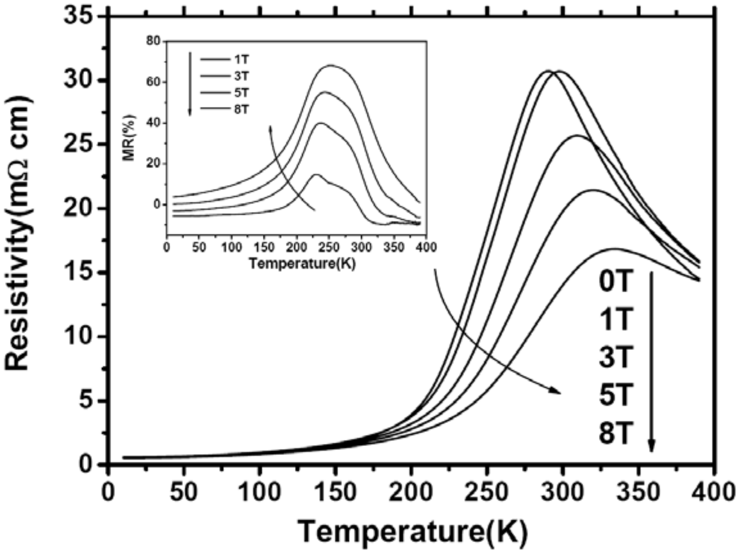

Figure 3.4: ρ(T) as a function of applied field for the PA LSnMO film. The inset illustrates the field dependence of the MR ratio.

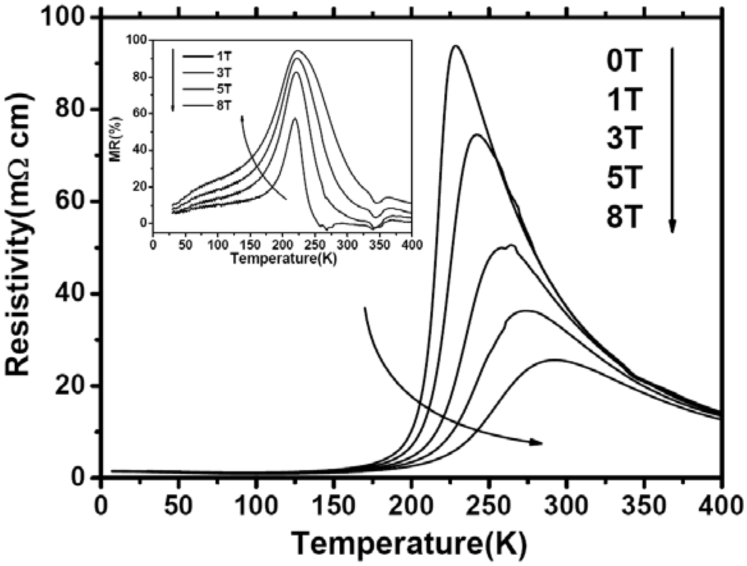

Figure 3.5: ρ(T) as a function of applied field for the ArPA LSnMO film. The inset illustrates the field dependence of the MR ratio.

3.2 Electronic structure

Fig. 3.6 shows the XAS results of Mn-$L_{2,3}$ for the AD-, PA-, and ArPA-films together with that of several “standard” powder samples. The results demonstrate that, while the AD-film indeed displays qualitative mixed-valence state characteristics of Mn^{2+}/Mn^{3+}, the valence state of Mn in the PA- and ArPA-films appears to be closer to that of the Mn^{3+}/Mn^{4+} mixed state. The manifestation of Mn^{2+} characteristic revealed in the XAS of the AD-film indicates that the PLD process, though may simultaneously introduce significant structural disorders, does help in retaining the Sn ions in the lattice. On the other hand, both the PA and ArPA processes appear to drive the LSnMO toward the hole-doped regime, except that there is signature of Mn^{2+} (the pre-edge peak around 640 eV) appearing for the latter. In order to further delineate the possible difference between the electronic structure of PA and ArPA films implied in the magneto-transport results described above, we show, in Fig. 3.7, the XAS of Sn together with that obtained from the standard samples of SnO_2 and SnS powder. We first note that the results essentially dismiss the existence of Sn^{2+} ions in the LSnMO films, despite it has been anticipated that the ionic size of Sn^{2+} (0.96Å) seems to be more favorable than that of Sn^{4+} (0.81Å) in substituting the La^{3+} (1.13Å) ions in the perovskite structure [30]. The XAS data of Sn in the PA-LSnMO (oxygen-annealed) films qualitatively demonstrate the features obtained from the standard SnO_2 samples, indicating that majority of Sn ions are in the valence state of Sn^{4+}. In comparison, the XAS of Sn in the AD film displays a smeared characteristic of Sn^{4+} around the same energy range. This is indicative that the Sn ions are residing on the La-sites and are either affected by the size-mismatch-induced strain or even participating the hybridization between Mn-3*d* and O-2*p* orbitals, as in this case most of Sn ions are retained in the La-Sn-Mn-O films (*vide infra*). On the contrary, the XAS data of Sn in the Ar-annealed film do not show the signature of either Sn^{2+} or Sn^{4+}, suggesting that the doped Sn in the initial target material may have been largely missing in the ArPA LSnMO film, at least within the depth probed by the XAS. We, thus, suspect that the magneto-transport properties demonstrated previously might be the manifestations of some La-deficient manganite derived from the argon-annealed process. Besides, the unambiguous Sn^{4+} feature observed in the PA-LSnMO films suggests that either the valence of Sn in LSnMO is really 4+ or there is some SnO_2 or other tin-compounds formed in the LSnMO sample during the oxygen annealing process. Although the high T_c and high T_{IM} exhibited by these films have indicated that the latter is more likely the case, direct evidence is desirable to clarify this issue.

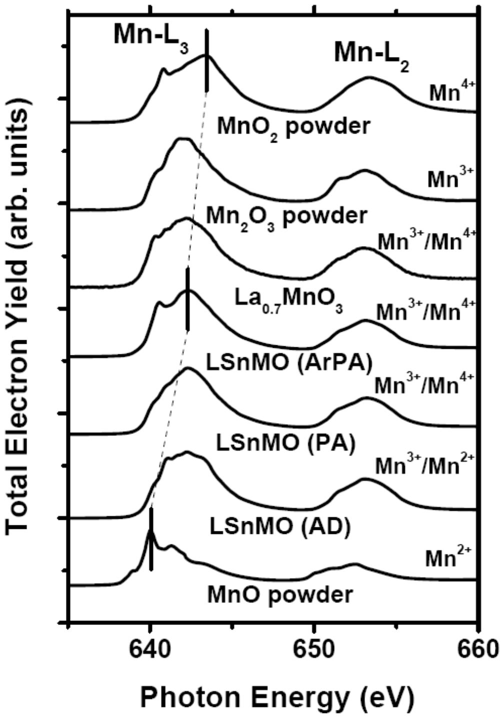

Figure 3.6: The x-ray absorption spectra of Mn-$L_{2,3}$ for LSnMO film. Spectra for various standard reference compounds are also displayed for comparison.

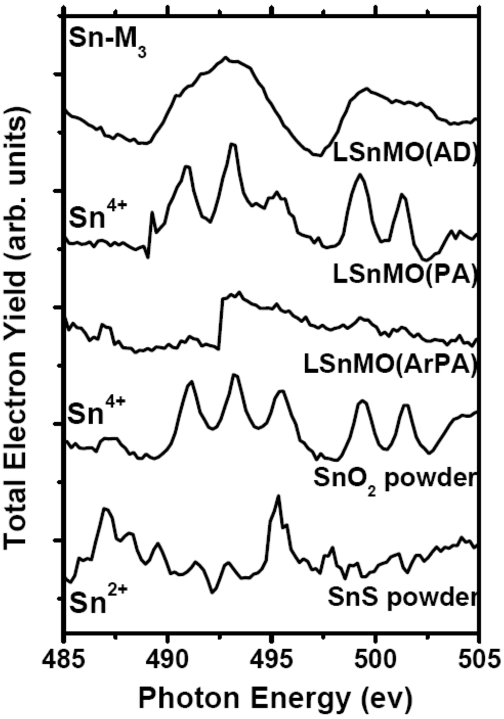

Figure 3.7: The x-ray absorption spectra of Sn-M_3 for LSnMO film. Spectra for various standard reference compounds are also displayed for comparison.

3.3 Microstructure and constituents distribution analysis

The energy dispersive spectroscopy analysis for AD and PA LSnMO films were as illustrated in Fig 3.5a and 5b. It reveal there are no difference between these two sample, suggesting the amounts of the four elements (La, Sn, Mn, O) do not change after the post annealing process. Fig. 3.8 compares the θ–2θ scan of x-ray diffraction (XRD) results for AD, ArPA and PA LSnMO films. As is evident from the results, all the films are c-axis oriented with no observable impurity phases. The slight split of the (00ℓ) peaks between the ArPA and PA-films and the substrates, however, indicates that significant strain relaxation may have occurred after prolonged annealing. To further delineate the possible subtle changes in the film microstructure due to annealing, L-scan and ϕ-scan measurements were performed. The typical results are illustrated in Fig. 3.9－3.11, respectively. In Fig. 3.9, it is evident that, in addition to the sharp Bragg peak from the LAO substrate, well-resolved (003)-reflection peaks of the LSnMO films were observed for the AD, ArPA, and PA samples with the correspondent c-axis lattice constant being 3.908Å, 3.893Å and 3.878 Å, respectively. Since the LSnMO film on LAO substrate is expected to experience an in-plane compressive stress due to the smaller substrate lattice constants, the progressive shortening of the c-axis lattice constant exhibited in the ArPA and PA films is indicative of the occurrence of annealing-induced strain relaxation, which in turn drives the film toward its bulk characteristics (The pseudocubic lattice parameter of $La_{1-x}MnO_3$ ranges from 0.3866 nm-0.3880 nm for $x = 0 – 0.33$ [25, 28].). We note that the in-plane lattice parameters also exhibited noticeable shrinkage upon annealing with a = 3.913Å, 3.907Å and 3.900Å for AD, ArPA, and PA films, respectively. Valencia *et al.* [32] pointed out, in their study of LCMO/STO films, that the existence of oxygen vacancies compensates the excessive elastic energy in coherently strained films. Thus, the shrinkage of the unit cell volume may reflect the elimination of oxygen vacancies and associated strain energy. The full width at the half maximum (FWHM) of the (0 –1 3) peak of AD-LSnMO is about 4.4°, which is much larger than that of LAO (103) (0.1°). This can be either due to the strain or fine grain size effects. The in-plane grain size estimated from the line width of K-scan across the LSnMO (0 –1 3) reflection is approximately 100 Å. On the other hand, for the PA film, the FWHM of LSnMO (103) is about 1.9°, which, though still much larger than that of LAO (103) (~0.036°), is significantly smaller than that observed in AD-film. The in-plane grain size as estimated from the line width of the H-scan across the LSnMO (103) reflection is approximately 135Å. This difference strongly suggests the crystallinity of LSnMO films was significantly improved upon annealing while the in-plane epitaxial relations remain largely intact. The ϕ-scans were taken along the (0 –1 3) Bragg peak of the LAO substrate and LSnMO films. As is evident from Figs. 3.10 and 3.11, both AD- and PA-LSnMO films display well-aligned ab-plane epitaxy with the LAO substrate. Again, the FWHM of the diffraction peaks for the AD-film is larger than that of the PA-film consistent with the arguments aforementioned for the XRD results.

To further delineate the evolving film/substrate relations due to annealing, Fig. 3.12—3.14 compares the reciprocal space maps of AD-, ArPA- and PA-LSnMO films. The decreasing peak position offset in $q_{||}$ between LAO and LSnMO in the reciprocal space maps clearly shows the occurrence of strain relaxation effect after annealing process. It is also evident that the lattice constants of LSnMO are significantly larger than that of LAO, consistent with the abovementioned results. For comparison, we show, in Fig. 3.15, the similar plot obtained for the PA LSnMO/STO (001). Since the lattice constant of LSnMO falls between STO and LAO and is closer to that of STO, LSnMO grown epitaxially on STO and LAO would experience a tensile/compressive average in-plane strain, respectively. In the case of LSnMO/STO, the films are fully coherent to the substrate, as indicated by the nearly perfect alignment between the center of the STO(113) and LSnMO(113) peak contours. Nevertheless, in both bases, we observe shrinkage of both the *c*-axis lattice constant and unit cell volume of LSnMO upon post-annealing; in LSnMO/STO case, *a*-*b* remains invariant but in the case of LSnMO/LAO, *a*-*b* also decreases slightly. It appears that some of the strain, originally compensated by oxygen vacancy incorporation [32], was released through the reduction of average unit cell volume. Alternatively, it is also possible that the change of average lattice parameters upon PA is coupled with change of composition, or even second-phase segregations. In any case, the lattice constant change associated relaxation of the strain in the films, though might originate from very different mechanisms, do intimately correlate to the enhanced CMR properties in a consistent manner. Unfortunately, the x-ray analyses seemed inadequate to precisely answer the question about the role played by Sn.

In order to further examine the distribution of Sn and the possibly formed Sn-compounds that are not discernable by using x-ray diffraction alone, we performed the cross-sectional transmission electron microscopy (X-TEM) analyses to reveal the microstructure and the element distribution of the LSnMO films. Fig. 3.16 and Fig. 3.17

show the bright-field TEM images and selective area diffraction (SAD) pattern of AD LSnMO(001) film grown on LAO(001) substrate. As can be seen from Fig. 3.16, the film microstructure appears to be rather homogeneous and there is no trace of any additional compound existing within the interface of film and substrate. In addition, the absence of extra diffraction spots in Fig. 3.17 indicates that the AD-LSnMO film grown on LAO substrate is indeed single phase with well-organized epitaxial relations. The rod-like diffraction spots and the streaky patterns appeared in the columnar grains of the LSnMO phase suggest that there exists a significant amount of strain in the film. We believe that both the slight lattice mismatch between the film and substrate and the large ionic size difference between La^{3+} and Sn^{4+} may contribute. For the PA-LSnMO film, however, the results are quite different. The bright field image shown in Fig. 3.18 apparently displays two somewhat separated regions. The grains in the near surface upper region appear to be more "equi-axial" with much less strain-induced streaky patterns, suggesting significant recrystallization may have occurred due to annealing. In the "lower" region (region close to the substrate interface) the features are more like that observed in the AD-film. Although it is still not obvious to conclude whether or not the recrystallized upper region containing any newly formed phases from the SAD results, it is, nevertheless, interesting to find that the oxygen annealing affects only the upper part of the film. With the about 4 hours of annealing time and 100 nm of the affected depth, the estimated oxygen diffusion rate at 800 °C is about 25 nm/hr.

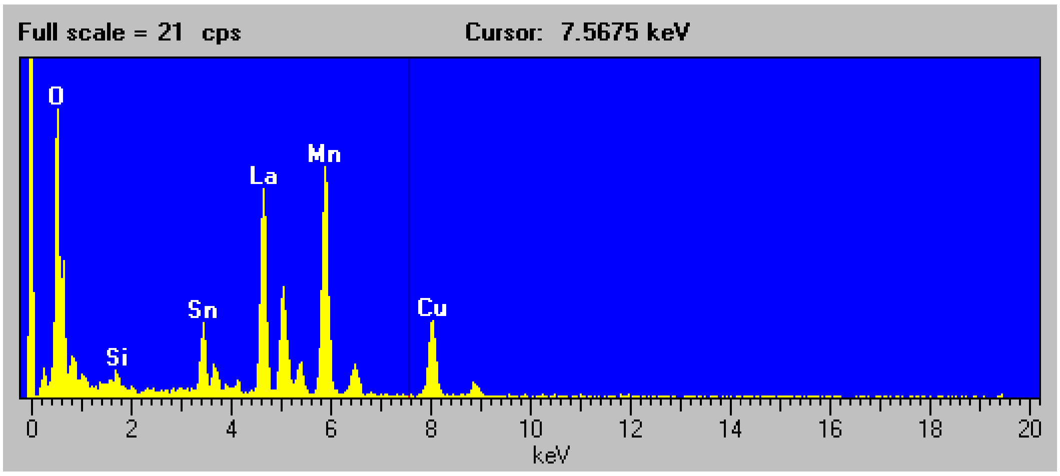

Figure 3.5a: The energy dispersive spectroscopy analysis (EDX) for AD LSnMO film.

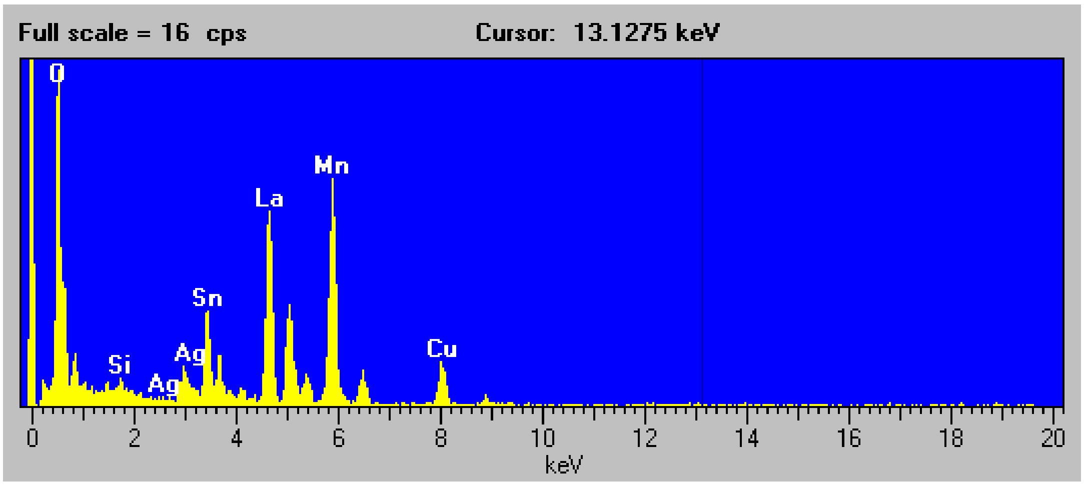

Figure 3.5b: The energy dispersive spectroscopy analysis (EDX) for PA LSnMO film.

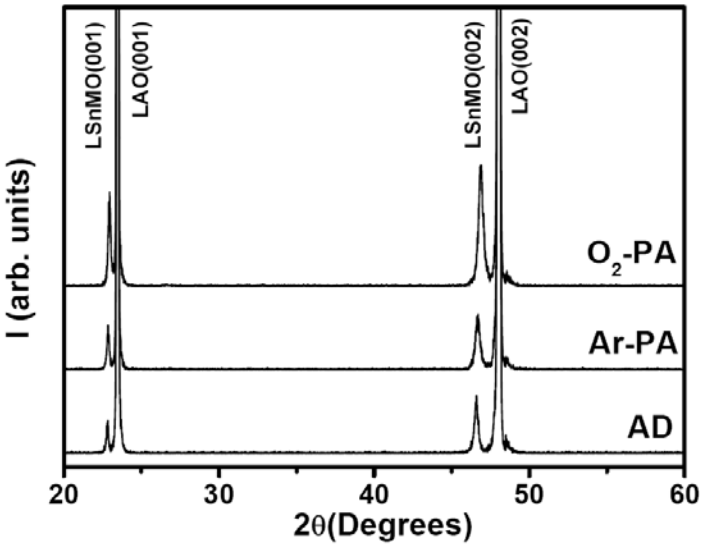

Figure 3.8: XRD results for the as-deposited, Ar-annealed and post-annealed LSnMO films grown on LAO substrates at $T_s = 780^oC$.

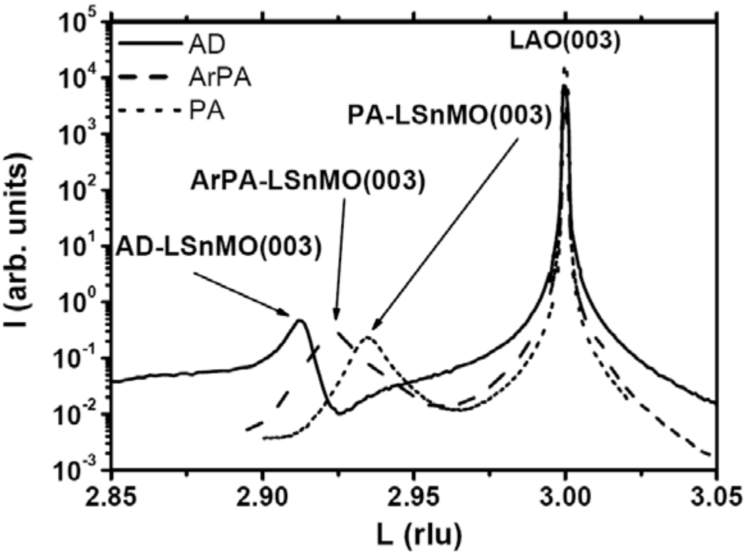

Figure 3.9: L-scan of AD, ArPA and PA films across (003) Bragg peak.

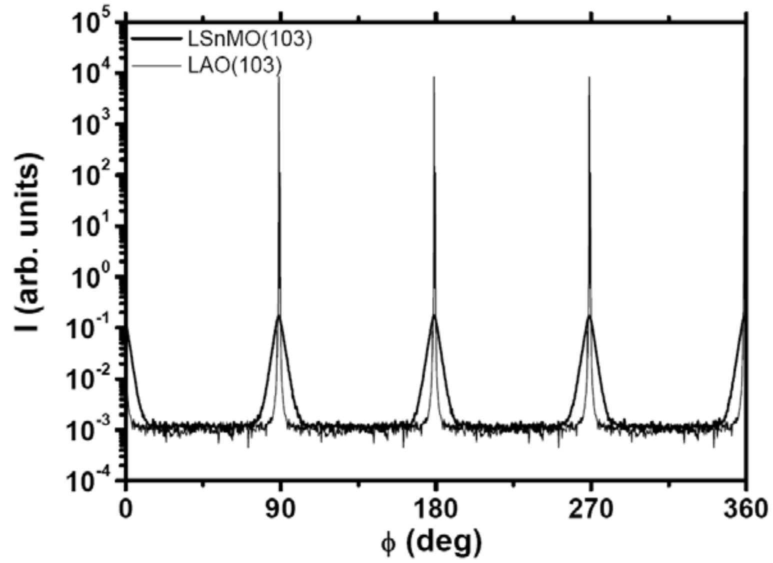

Figure 3.10: The ϕ-scans for the LAO (103) and AD LSnMO (103) Bragg peaks, respectively.

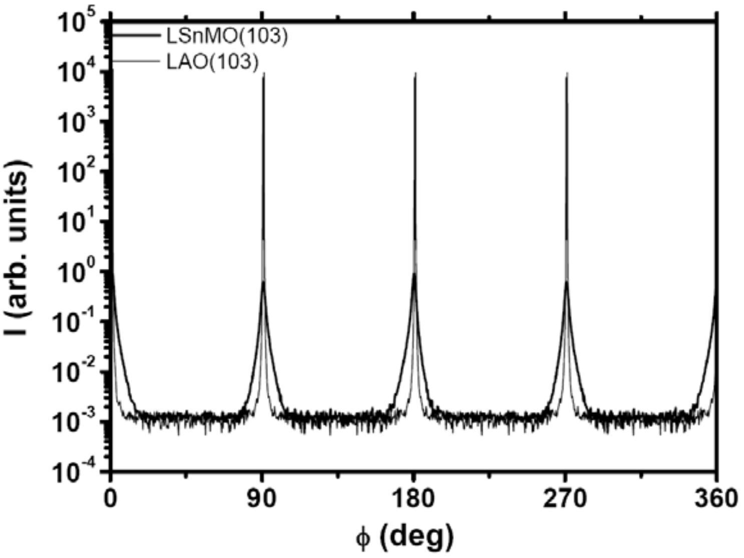

Figure 3.11: The ϕ-scans for the LAO (103) and PA LSnMO (103) Bragg peaks, respectively.

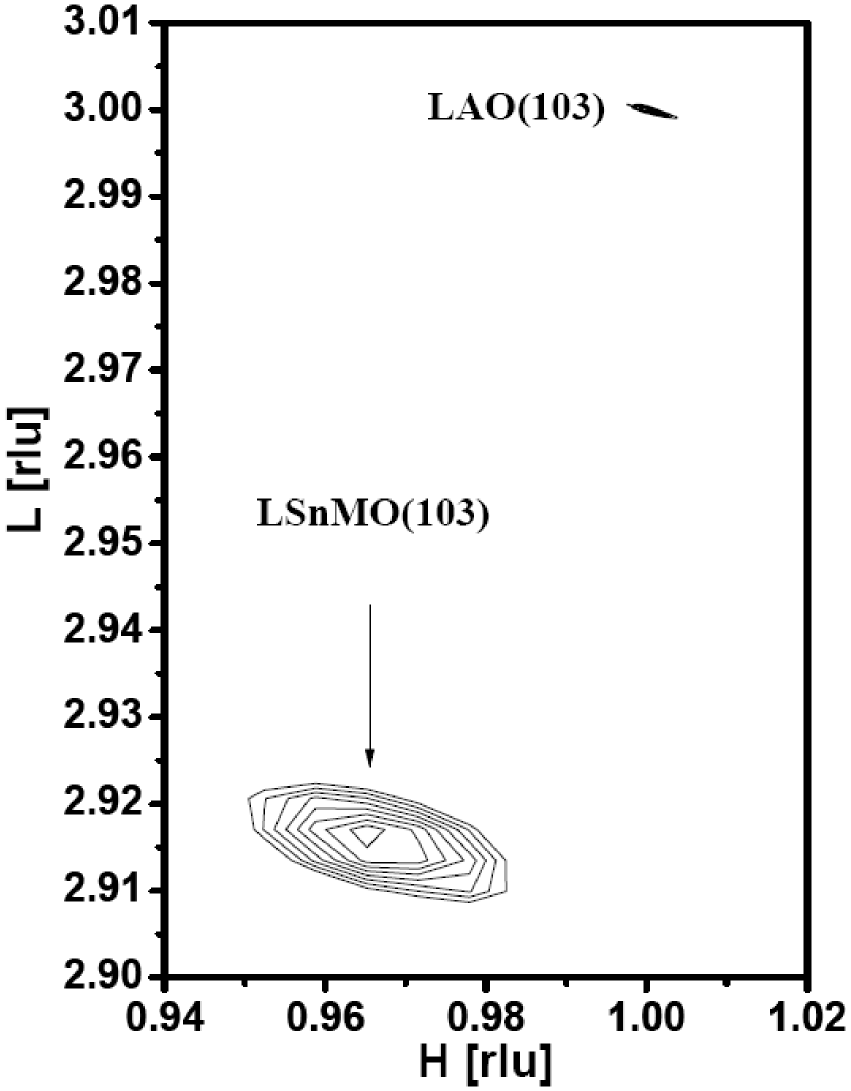

Figure 3.12: Reciprocal space maps of AD LSnMO films grown on LAO substrate.

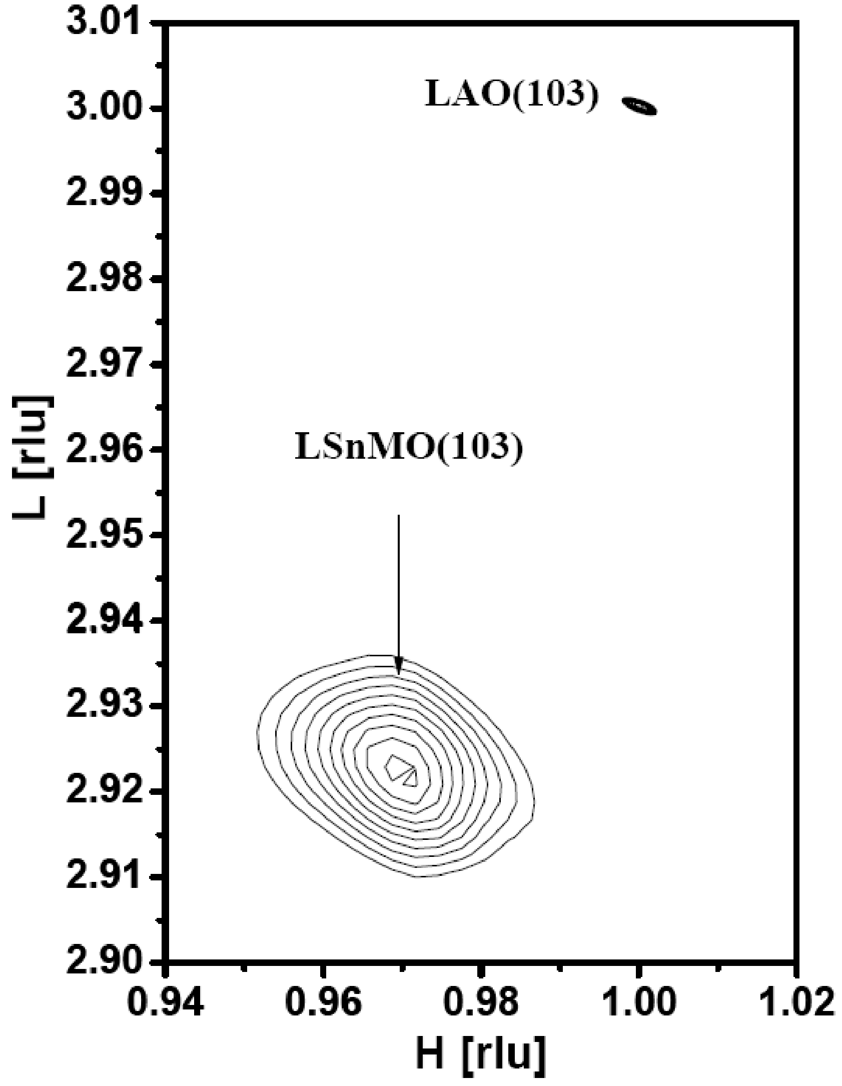

Figure 3.13: Reciprocal space maps of ArPA LSnMO films grown on LAO substrate.

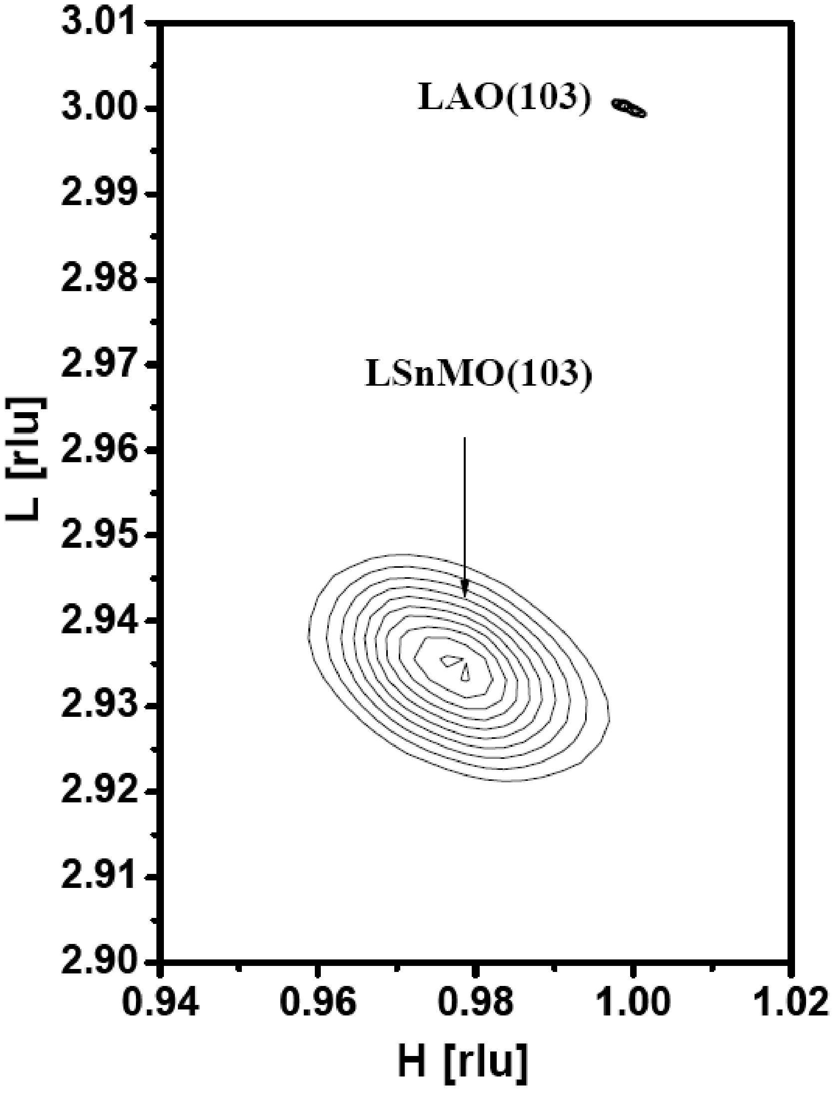

Figure 3.14: Reciprocal space maps of PA LSnMO films grown on LAO substrate.

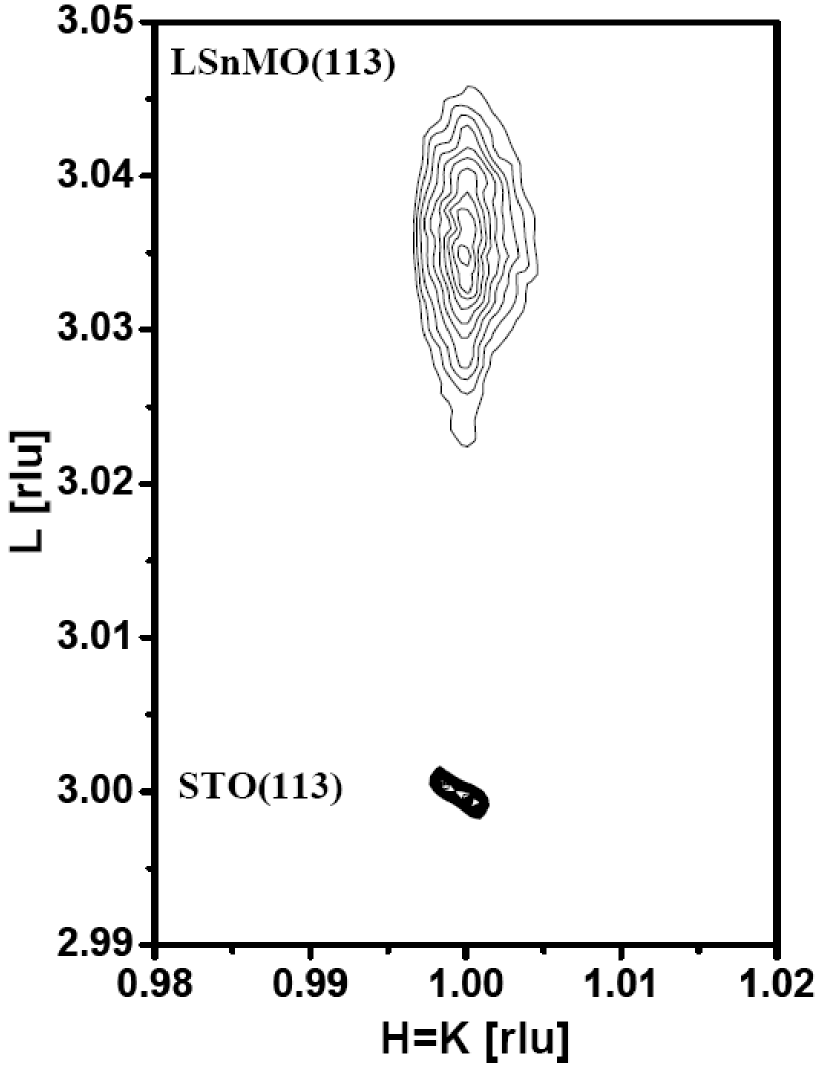

Figure 3.15: Reciprocal space map of PA LSnMO film grown on STO substrate.

From the above discussion, the strain relaxation effect is consistent with what observed in x-ray diffraction analyses and hence account for part of the magneto-transport properties obtained. The XAS results, however, remain to be clarified. In order to delineate the effect of annealing on the composition distribution of the doped element in the LSnMO film, the electron energy loss spectroscopy (EELS) mapping was performed on the TEM samples. Figs. 20(a1)-(a5) show the zero-loss image of the AD-LSnMO film and the elemental maps of La, Sn, Mn, O, respectively. As revealed by the series of the images, the four constituents distribute uniformly over the entire AD-LSnMO film, indicating that they are presumably situated within the parent perovskite structure. The results are largely consistent with the data discussed above. Nevertheless, the elemental maps of the four constituent elements in the PA-LSnMO film display rather different results. As illustrated in Figs. 20(b1)-(b5), there are clear evidence of local segregation of Sn and O in the "upper" region of the PA-LSnMO film (Fig. 20(b3) and (b5)). More interestingly, in these Sn-O segregated areas, both La and Mn are absent (Fig. 20(b2) and (b4)), indicating that the clusters formed are some kind of Sn-O compound. (From the previous XAS results it should be SnO_2.) This strongly implies that the oxygen annealing affected regions may indeed induce the formation of the La-deficient manganite, which, in turn, accounts for the marked enhancement in T_c and T_{IM} for the PA-LSnMO films described above.

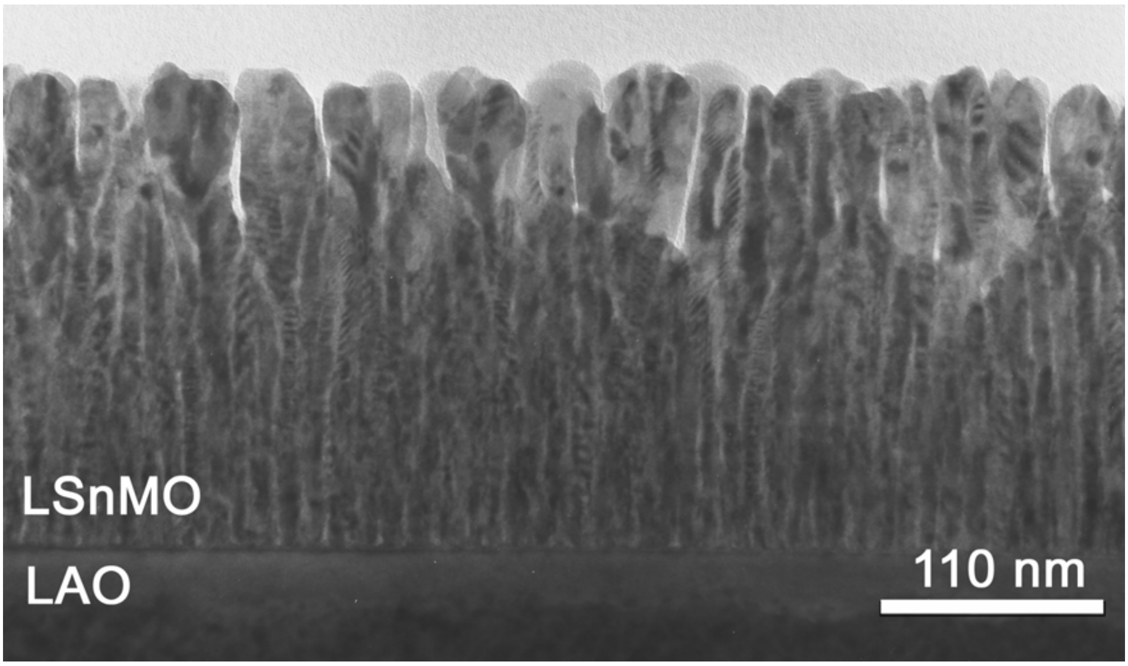

Figure 3.16: The bright-field TEM image for the AD LSnMO (001) film.

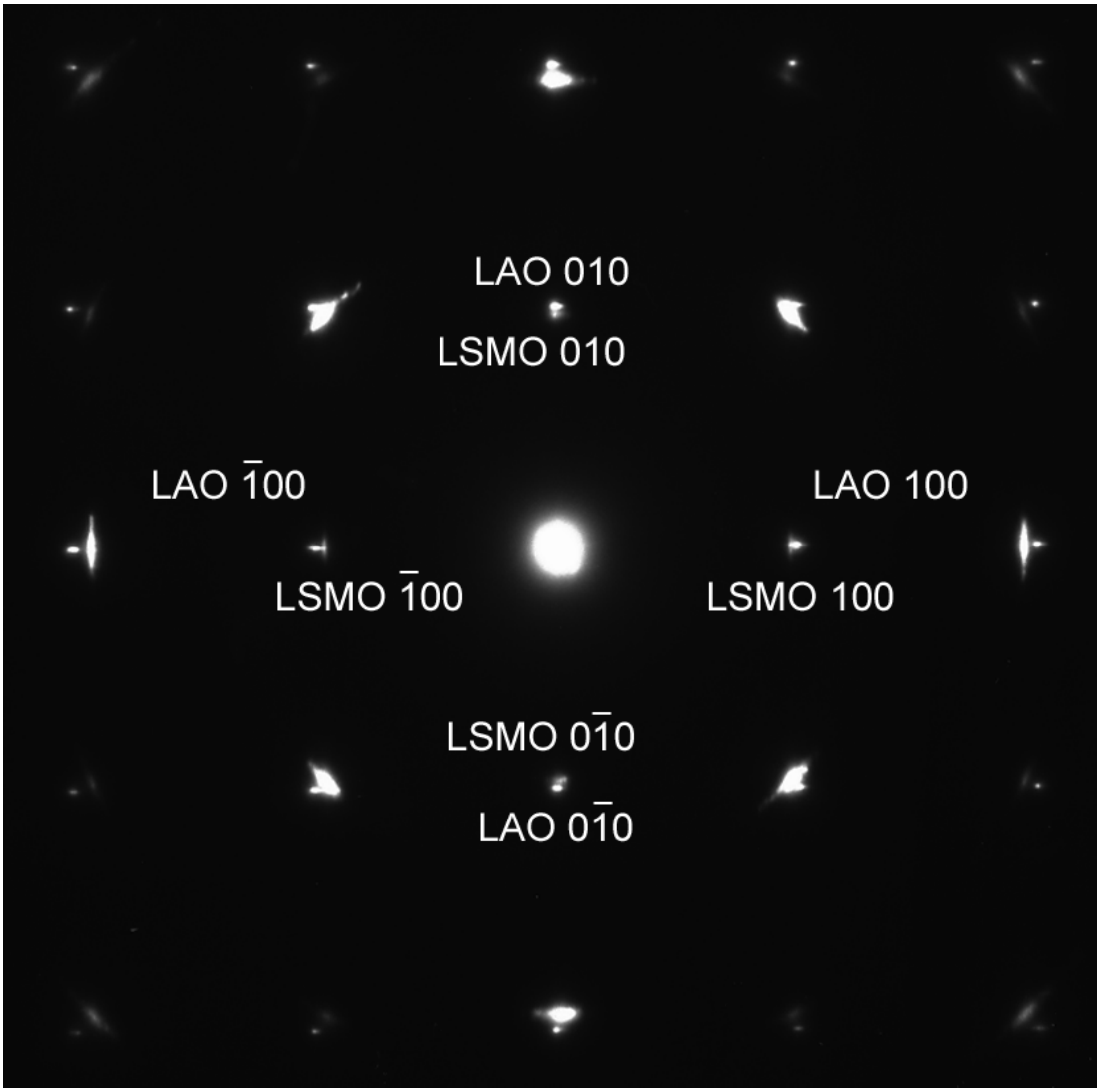

Figure 3.17: The electron diffraction pattern for the AD LSnMO (001) film.

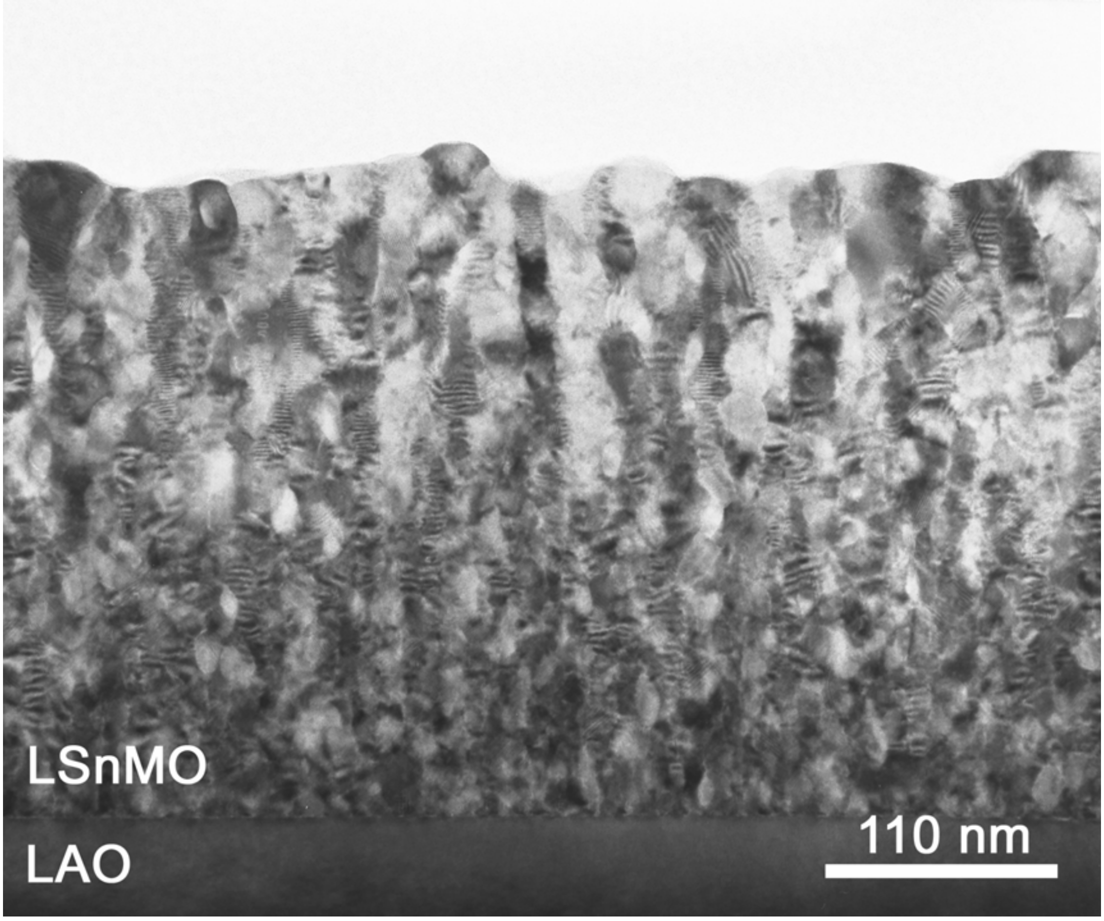

Figure 3.18: The bright-field TEM image for the PA LSnMO (001) film. Notice that the near-surface upper part of the PA LSnMO film displays apparent recrystallization signature upon prolonged annealing.

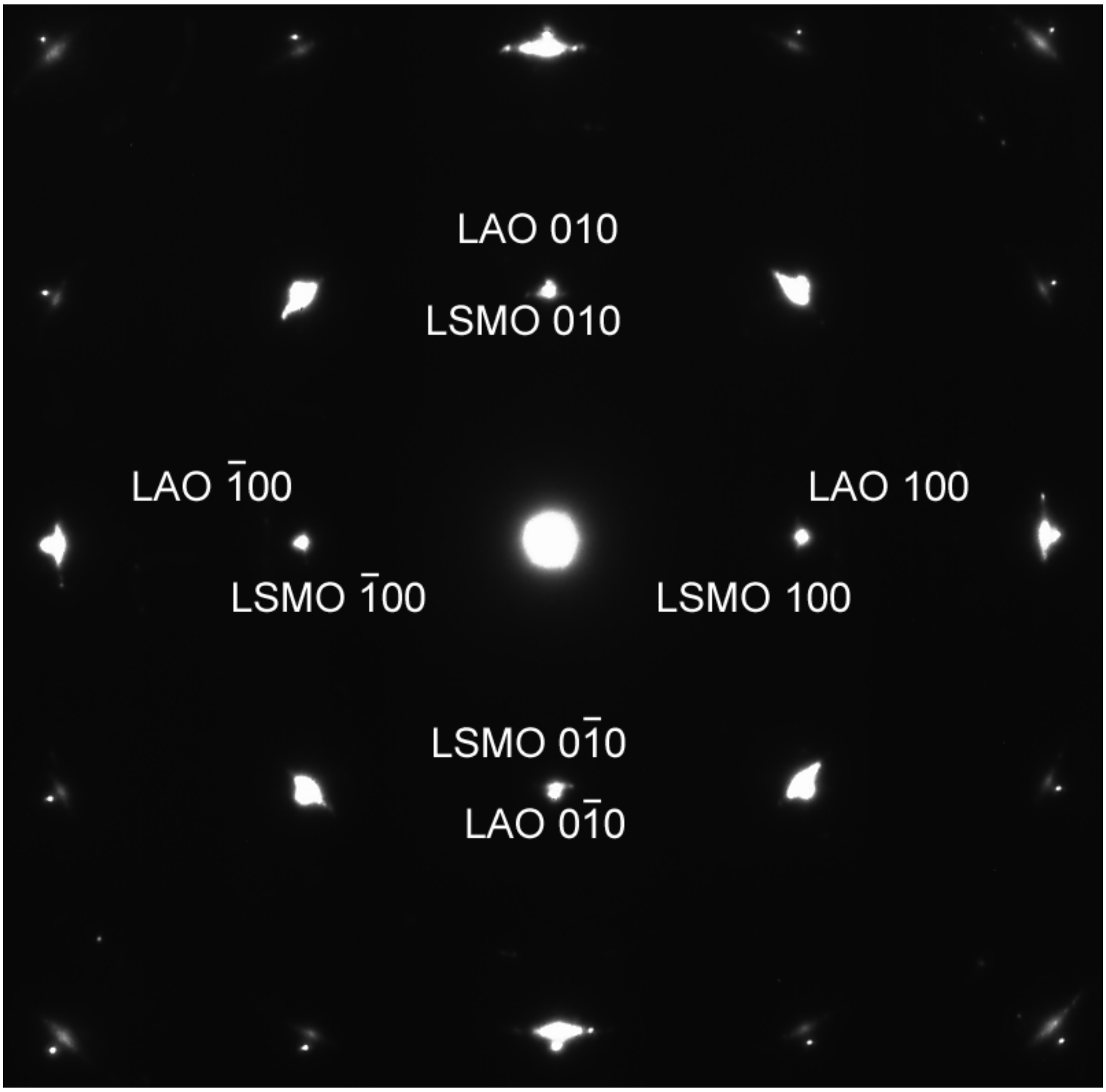

Figure 3.19: The electron diffraction pattern for the PA LSnMO (001) film.

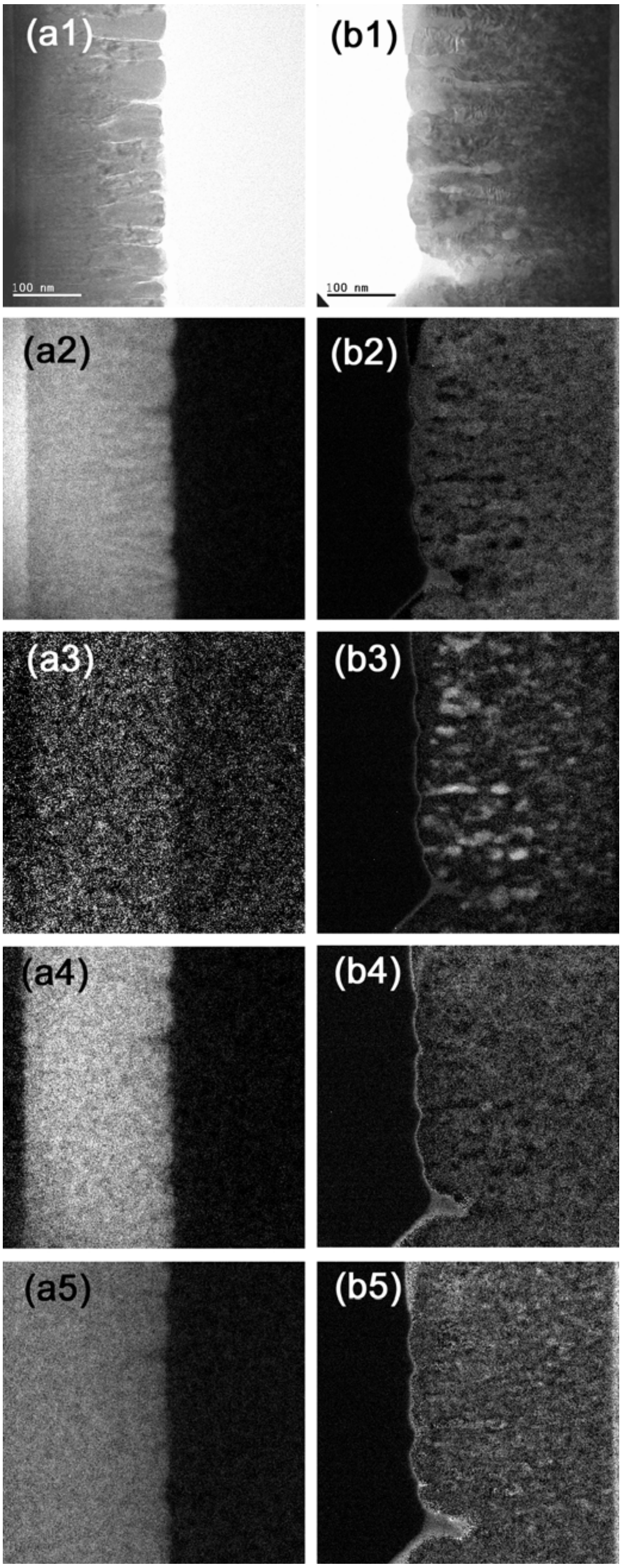
(a1)
(b1)
100 nm
100 nm
(a2)
(b2)
(a3)
(b3)
(a4)
(b4)
(a5)
(b5)

Figure 3.20: (a) The electron energy loss spectroscopy of the zero-loss image (a1) and the elemental maps of La (a2), Sn (a3), Mn (a4), and O (a5) of the AD LSnMO film. (b) The electron energy loss spectroscopy of the zero-loss image (b1) and the elemental maps of La (b2), Sn (b3), Mn (b4), and O (b5) of the PA LSnMO film.

3.4 Discussion

In the following, we try to put the experimental observations presented above together to see if it can be reconciled to the outstanding issues about the CMR effects on Sn-doped manganites that we set forth to resolve at the beginning. The very first question to be answered is whether or not Sn-ions can substitute La-sites? The results obtained from the as-deposited films indicated that the substitution of the tetravalent Sn into the La site does prevail and result in a ferromagnetic-insulating manganite. The unexpected insulating behavior thus suggests either the lack of itinerant carriers or a fundamentally different exchange mechanism in the electron-doped regime. In the former scenario, similar double-exchange mechanism as in the hole-doped manganites gives rise to the paramagnetic-ferromagnetic transition and the existence of Mn^{2+} due to tetravalent doping of Sn^{4+} should result in enhancement of saturation magnetization below T_c owing to contributions from extra e_g electrons. However, due to the charge localization effects associated with strain-induced lattice distortion, the lack of itinerant electrons not only has hindered effective transport but also is responsible for the absence of long range FM order as manifested in the dramatic reduction of saturation magnetization and marked spin-glass-like behavior displayed in Fig. 3.1—3.3. The large epitaxial strain originally existent in the AD-film as revealed by the x-ray and X-TEM analyses seemed to give consistent support. On the other hand, the existence of Mn^{2+} in as-deposited and prolonged air exposure LCMO films was found to yield charge localization, and hence increasing resistivity and reducing magnetization, as well.[25] However, the effects of Mn^{2+}-induced charge localization seemed too modest to drive it into ferromagnetic insulator. Another possibility for explaining why our AD LSnMO films present as a ferromagnetic insulator is that the doping level ($x = 0.3$) is too low to drive the LSnMO into n-type manganite. Chang *et al.* [12] indicated that the one of the main effects of doping Ce (up to $x = 0.3$) into $LaMnO_3$ was to dramatically shrink the hole-pockets near the Fermi level, instead of providing itinerant electrons and driving LCeMO into a n-type manganite. We believe that, from the evidence exhibited by XAS (especially on Sn ion) and EELS of XTEM analyses, for AD-LSnMO films, effective doping is obtained. However, the tetravalent- doping-induced hole-pocket shrinkage effects similar to that observed in Ce-doped manganites [12] may also happen in the present AD-LSnMO films. Together with the influences of the coherent strain and, possibly larger ion-size effect, thus resulted in the ferromagnetic insulating as well as spin-glass-like behaviors displayed by the AD-LSnMO films.

On the other hand, although post annealing under oxygen or argon is usually practiced in the fabrication of the “electron-doped” manganites, our experimental results demonstrate that it may not work as expected. According the XAS of Sn, we are tempted to rule out the existence of Sn^{2+} ions in the LSnMO films. The XAS of Sn for the PA-LSnMO film evidently shows the characteristics of Sn^{4+} valence. On the contrary, the same spectrum for the Ar-annealed film does not show the characteristics of either Sn^{2+} or Sn^{4+}, suggesting that the doped Sn in the initial target material may have been largely missing in the ArPA-LSnMO film. The question is how do these spectrum results correlated to the magneto-transport properties displayed by the respective films? The TEM microstructure analyses and the EELS elemental map of PA-LSnMO film evidently showed that there is some kind of Sn-O compound formed during the post-annealing. The unambiguous Sn^{4+} feature of XAS results strongly implies that within the oxygen annealing affected regions it may have indeed induced the formation of the La-deficient manganite with SnO_2 clusters. The significant improvement of the CMR effects, including high T_c, T_{IM}, low resistivity and relatively large magnetization at low temperatures, is naturally explained within the context of this scenario. Finally, for the ArPA-LSnMO films, although also exhibit transitions from paramagnetic insulator to ferromagnetic metal albeit at a significantly lower temperature with higher resistivity, the detailed mechanism may be fundamentally different from the oxygen-annealed PA-LSnMO films. In particular, the XAS of Sn for this film showed most of the Sn was missing after annealing. Thus, although the reduced average unit-cell volume for the ArPA- and PA-LSnMO films is indicative of strain relaxation, it is doubtful to attribute it as the sole reason for the obtained enhancement on the magneto-transport properties. It is quite possible that the change of average lattice parameters upon annealing is also coupled with change of composition, or even segregation of second phases. In this scenario, the excessive oxygen presumably present in the PA-LSnMO films would provide more itinerant carriers and Mn^{4+} content[32], and is responsible for the improvement of electrical transport and magnetic properties. While Ar-annealing, though may induce the loss of Sn and hence result in La-deficient manganite, it may also provoke the formation of non-ferromagnetic Mn^{2+} component and give rise to charge localization-induced increase in resistivity and reduction in saturated magnetization [25].

Finally, we make a brief comparison between LSnMO and LCeMO, the two representative “electron-doped” manganites. The primary distinction of these two materials is the ionic size difference of Sn^{4+} (0.81Å) and Ce^{4+} (0.97Å) [31]. One of the instant effects resulted from this was the low temperature saturation magnetization obtained from the as-deposited films with $M_{\mathrm{LCeMO}} \sim 1.4\mu_B$/Mn-site [13] and $M_{\mathrm{LSnMO}} \sim 0.4\mu_B$/Mn-site measured under T＝10K, H＝100Oe. This may be easily attributed to more severe structure disorder originated from the larger ionic size difference between Sn^{4+} and La^{3+} (0.32Å) than that between Ce^{4+} and La^{3+} (0.16Å). However, as the films were annealed under oxygen environment, both LSnMO and LCeMO exhibit similar magneto-transport properties. The existence of SnO_2 or CeO_2 [13] seemed to indicate that both films tend to turn into La-deficient manganites after annealing. However, for as-deposited PLD LCeMO films, there are still some discrepancies on the magneto-transport properties reported in the literature remained to be clarified [9-13].

4. Summary

In summary, we have presented systematic investigations on one of the highly anticipated electron-doped CMR materials. Single-phase $La_{0.7}Sn_{0.3}MnO_3$ (LSnMO) thin films were grown on $LaAlO_3$ substrates by pulsed laser deposition. The as-deposited LSnMO films are ferromagnetic insulators with typical Curie temperature around 150 K. Both the electronic structure revealed by the x-ray absorption spectra (XAS) and the detailed TEM analyses indicate that in this case the doped Sn-element is indeed acting as the tetravalent ion uniformly distributed in the $LaMnO_3$ parent compound. The large internal strain originated from the marked ion size difference between the doped Sn^{4+} and substituted La^{3+} ions, however, is believed to hinder the long-range itinerancy of the carriers, hence preventing it from becoming metallic. Unfortunately, due to the insulating nature of these as-deposited LSnMO films, it is not clear whether it is indeed “n-type” electron-doped manganite. *Ex-situ* annealing in oxygen and argon both drive the films to exhibit insulator-metal transition with hole-doped characteristics when becoming ferromagnetic. The transition temperatures, however, are different for films annealed in different environments, presumably due to the final phase and compositions obtained. From the results of magnetoresistance measurements and XAS, it is suggestive that LSnMO films annealed in argon causes the significant loss of Sn and results in La-deficient phase. Whereas those annealed in oxygen appeared to form some kind of Sn-O compound, turning the films into La-deficient manganite, albeit with some excessive oxygen. We emphasize that the existence of tetravalent Sn from x-ray absorption spectroscopy (XAS) should not be taken as the sole evidence of achieving electron-doped manganite. As being clearly demonstrated in this study, it may just reveal the emergence of SnO_2.

References

[1] Y. Tokura and N. Nagaosa, Science **288**, 462 (2000), and references therein.

[2] E. Dagotto, “*Nanoscale Phase Separation and Colossal Magnetoresistance*” (Springer, 2003), and references there in.

[3] C. Zener, Phys. Rev. **82**, 403 (1951).

[4] A.J. Millis, P.B. Littlewood, B.I. Shraiman, Phys. Rev. Lett. **74**, 5144 (1995).

[5] V. L. Joseph Joly, P. A. Joy, S. K. Date, J. Magn. Magn. Mater. **247**, 316 (2002).

[6] S. Das and P. Mandal, Z. Phys. B **104**, 7 (1997); P. Mandal and S. Das, Phys. Rev. B **56**, 15073 (1997).

[7] A. Gupta, T. R. McGuire, P. R. Duncombe, M. Rupp, J. Z. Sun, W. J. Gallagher, and Gang Xiao, Appl. Phys. Lett. **67**, 3494 (1995).

[8] S. Pingard, H. Vincent, J. P. Senateur, J. Pierre, and A. Abrutis, J. Appl. Phys, **82**, 4445 (1997).

[9] C. Mitra, P. Raychaudhuri, J. John, S.K. Dhar, A.K. Nigam, and R. Pinto, J. Appl. Phys. **89**, 524 (2001).

[10] W. J. Chang, C. C. Hsieh, J. Y. Juang, K. H. Wu, T. M. Uen, Y. S. Gou, C. H. Hsu, and J.-Y. Lin, J. Appl. Phys. **96, 4357** (2004).

[11] T. Yanagida, T. Kanki, B. Vilquin, H. Tanaka, and T. Kawai, Solid State Comm. **129**, 785 (2004).

[12] W. J. Chang, J. Y. Tsai, H.-T. Jeng, J.-Y. Lin, Kenneth Y.-J. Zhang, H. L. Liu, J. M. Lee, J. M. Chen, K. H. Wu, T. M. Uen, Y. S. Gou, and J. Y. Juang, Phys. Rev. B **72**, 132410 (2005).

[13] Takeshi Yanagida, Teruo Kanki, Bertrand Vilquin, Hidekazu Tanaka, and Tomoji

Kawai, Phys. Rev. B **70**, 184437 (2004).

[14] Guotai Tan, X. Zhang and Zhenghao Chen, J. Appl. Phys. **95**, 6322 (2004).

[15] Ping Duan, Zhenghao Chen, Shouyu Dai, Yueliang Zhou, Huibin Lu, Kuijuan Jin, and Bolin Cheng, Appl. Phys. Lett. **84**, 4741 (2004).

[16] J. Gao, S. Y. Dai, and T. K. Li, Phys. Rev. B **67**, 153403 (2003).

[17] X. Guo, S. Dai, Y. Zhou, G. Yang, and Z. Chen, Appl. Phys. Lett. **75**, 3378 (1999).

[18] X. Guo, Z. Chen, S. Dai, Y. Zhou, R. Li, H. Zhang, B. Shen, and H. Cheng, J. Appl. Phys. **88**, 4758 (2000).

[19] J. A. Mydosh. *Spin Galsses: an Experimental Introduction*. Taylor & Francis, Lodon, 1993.

[20] S. de Brion, F. Ciorcas, G. Chouteau, P. Lejay, P. Radaelli, and C. Chaillout, Phys. Rev. B **59**, 1304 (1999).

[21] T. Y. Cheng, C. C. Hsieh, J. Y. Juang, J.-Y. Lin, K. H. Wu, T. M. Uen, Y. S. Gou, C. H. Hsu, Physica B **365**, 141 (2005).

[22] M. R. Ibarra, P. A. Algarabel, C. Marquina, J. Blasco, and J. García, Phys. Rev. Lett. **75**, 3541(1995).

[23] P. G. Radaelli, D. E. Cox, M. Marezio, S.-W. Cheong, P. E. Schiffer, and A.P. Ramirez, Phys. Rev. Lett. **75**, 4488 (1995).

[24] J. M. De Teresa, M. R. Ibarra, J. García, J. Blasco, C. Ritter, P.A. Algarabel, C. Marquina, and A. del Moral, Phys. Rev. Lett. **76**, 3392 (1996).

[25] S. Valencia, A. Gaupp, W. Gudat, Ll. Abad, Ll. Balcells, A. Cavallaro, B. Martínez, and F.J. Palomares, Phys. Rev. B **73**, 104402 (2006).

[26] S. J. Kim, C. S. Kim, S. I. Park, and B. W. Lee, J. Appl. Phys. **89**, 7416 (2001).

[27] B. C. Hauback, H. Fjellvag, and N. Sakai, J. Solid State Chem. **124**, 43 (1996).

[28] G. J. Chen, Y. H. Chang, and H. W. Hsu, J. Magn. Magn. Mater. **219**, 317 (2000).

[29] R. Suryanarayanan, J. Berthon, I. Zelenay, B. Martínez, X. Obradors, S. Uma, and E. Gemelin, J. Appl. Phys. **83**, 5264 (1998).

[30] K. A. Thomas, P. S. I. P. N. de Silva, L. F. Cohen, A. Hossain, M. Rajeswari, T. Venkateson, R. Hiskes, and J. L. MacManus-Driscoll, J. Appl. Phys. **84**, 3939 (1998).

[31] R. D. Shannon, Acta Crystallogr. A **32,** 752 (1976).

[32] S. Valencia, Ll. Balcells, J. Fontcuberta, and B. Martínez, Appl. Phys. Lett. **82**, 4531 (2003).

III、Future work

複雜的 Perovskite 的多鐵錳氧化物薄膜具有豐富的物理特性，是一種同時有鐵磁性質、鐵電性質的強關連電子系統。經由鐵磁極化（ferromagnetic polarization）與鐵電極化（ferroelectric polarization）彼此耦合（coupling），同時與晶格的耦也扮演了重要的角色，創造出豐富新穎的物理現象。因此，這樣的材料具有製備一高效能元件的高度潛力，同時也吸引了很多研究人員的注意，相關研究也日益增多。因此我們可藉由薄膜成長機制的研究，深入了解 Perovskite 結構薄膜成長的機制與特性。

我們未來主要研究多鐵錳氧化物薄膜的特性與摻雜金屬離子對於材料中鐵磁與鐵電性質所造成的改變。源自於對龐磁阻錳氧化物薄膜的豐富經驗，我們期許經過摻雜，可以提供載子在多鐵錳氧化物中扮演電性傳輸的角色，進一步發展出新穎豐富的物理現象。未來將製備出多鐵錳氧化物薄膜並進一步摻雜金屬離子以期能改變其晶格結構與電子組態，並深入探討不同 perovskite 結構（orthorhombic 與 hexagonal）成長相關的理論。並以 XRD、STM、AFM 檢驗所製作薄膜的軸向與結構，同時與同步輻射中心合作以 X 光探測表面乃至深層及介面間的差異性。進一步地利用這些分析數據控制成長出高品質的薄膜。研究使用外加電場與磁場量測其鐵電與鐵磁性質。利用各種不同材料摻雜的物理特性，完成不同混成結構的多種樣品，藉以比較晶格結構改變與組成變化對於多鐵錳氧化物薄膜中鐵電與鐵磁區域耦合作用的影響。製備樣品，以所建立的量測技術，探討不同材料的介面特性。我們將會評估製作多鐵錳氧化物元件，最後嘗試縮小尺寸以探討次微米尺度的臨界尺度，探

討相分離等重要物理現象，在尺寸效應下所受的影響。這除了在元件應用功能上，有基本的重要性之外，更可以進一步解析，多鐵物質中相共存的物理機制。預期未來將可對此一凝態物理中極重要的課題，做出具體的貢獻。參予研究的學生及其他研究人員，也將因此獲得寶貴的研究經驗與獨立進行研究的訓練。

Publication list

1. P.I. Lin, C.W. Luo, H.S. Liu, S.F. Chen, K.H. Wu, **J.Y. Juang**, T.M. Uen, Y.S. Gou, and J.Y. Lin, “On the origin of photogenerated terahertz radiation from current-biased superconducting YBCO thin films”, J. Appl. Phys. **95**, 8046 (2004).
2. C.W. Lin, T.Y. Cheng, L. Chang, and **J.Y. Juang**, “Chemical vapor deposition of zinc oxide thin films on Y_2O_3/Si substrates”, Phys. Stat. Sol.(c) **1**, 851 (2004).
3. H.K. Zeng, A. Hsiao, W.-H. Hsu, S.-W. Wu, J.-Y. Lin, K.H. Wu, **J.Y. Juang**, T.M. Uen, Y.S. Gou, and J.-T. Kuo, “Miniaturized 3 GHz Cross-Coupled Planar Microwave Filters”, IEEE Trans. Appl. Supercond. **14**, 107 (2004).
4. L. S. Lai, **J. Y. Juang**, K. H. Wu, T. M. Uen, Y. S. Gou, Physica C **133-138**, 415 (2004).
5. W.J. Chang, C.C. Hsieh, **J.Y. Juang**, J.Y. Lin, K.H. Wu, T.M. Uen, and Y.S. Gou, “Preparation and magneto-transport properties of single-phase electron-doped $La_{0.7}Ce_{0.3}MnO_3$ films”, accepted for publication by J. Appl. Phys. 96, 8 (2004).
6. T.C. Wang, **J.Y. Juang**, K.H. Wu, T.M. Uen, and Y.S. Gou, “Thermally activated diffusion observed by in-situ RHEED intensity monitoring on interrupted SrTiO3 homoepitaxial growth”, Jpn. J. Appl. Phys. **43**, 771 (2004).
7. T.C. Wang, J.Y. Lee, C.C. Hsieh, **J.Y. Juang**, K.H. Wu, T.M. Uen, and Y.S. Gou, “Activated kinetics of room temperature deposited SrTiO3 thin films investigated by RHEED monitored annealing with different heating rates”, accepted for publication by Jpn. J. Apply. Phys., July, (2004).
8. T.C. Wang, J.Y. Lee, **J.Y. Juang**, K.H. Wu, T.M. Uen, and Y.S. Gou, “RHEED in-situ monitored step edge diffusion during interrupted laser ablation epitaxial growth of SrTiO3”, accepted for publication by Chin. J. Phys., July, (2004).
9. Te-Chun Wang, Jung-Yuee Lee, Chih-Chang Hsieh, **Jenh-Yih Juang**, Kaung-Hsiung Wu, Tzeng-Ming Uen and Yih-Shun Gou, Jpn. J. Apply. Phys. 44, 1067-1068 (2005).
10. C. W. Lou , M. H. Chen , S. P.Chen , K. H. Wu , **J. Y. Juang** , J. –Y. Lin , T. M. Uen , and Y. S. Gou :“ Symmetry and doping dependence of the two

superconducting gaps of underdoped textured $YBa_2Cu_3O_{7-\delta}$ thin films " , submitted to Physical Review B (2005).

11. C. W. Lou , P. T. Shih , Y. -J.Chen , M. H. Chen , K. H. Wu , **J. Y. Juang** , J. –Y. Lin , T. M. Uen , and Y. S. Gou :"Spatially-resolved relaxation Dynamics of Photoinduced Quasiparticle in Underdoped $YBa_2Cu_3O_{7-\delta}$", Physical Review B **72**, 092506 (2005).
12. P. I. Lin, K. H. Wu, **J. Y. Juang**, J.-Y. Lin, T. M. Uen, and Y. S. Gou, "Generation of THz Radiation and Its Application in the Studies of Electrodynamics of High-Tc Superconductors in THz Regime", 2005 Japan-Taiwan Symposium on Superconductive Electronics, Sapporo, Japan, Feb. (2005).
13. Chih-Wei Lin, Tsan-Yao Cheng, Li Chang, **Jenh-Yih Juang**, J.Crystal Growth **50**, e2481–e2485 (2005).
14. T. Y. Cheng, C. C. Hsieh, **J. Y. Juang**, J.Y-.Y Lin, K. H. Wu, T. M. Uen, Y. S. Gou, C. H. Hsu, Physica B 141-146, 365 (2005).
15. H. Chou, Z. Y. Hong, S. J. Sun, **J. Y. Juang**, and W. J. Chang, " Strong anisotrpoic maganetoresistance and magnetic interaction in $La_{0.7}Ce_{0.3}MnO_3/La_{0.7}Ca_{0.3}MnO_3$ p-n junction.", J. Appl. Phys **97**, 10A308 (2005).
16. W. J. Chang, J. Y. Tsai, H.-T. Jeng, J.-Y. Lin, Kenneth Y.-J. Zhang, H. L. Liu, J. M. Lee, J. M. Chen, K. H. Wu, T. M. Uen, Y. S. Gou, and **J. Y. Juang**, Phys. Rev. B **72**, 132410 (2005).
17. L. S. Lai, **J. Y. Juang**, K. H. Wu, T. M. Uen, Y. S. Gou, Physica C **99-103**, 432 (2005).
18. L.S. Lai , H.K. Zeng, **J.Y. Juang**, K.H. Wu, T.M. Uen, J.Y. Lin, Y.S. Gou, "Physical properties of $YBa_2Cu_3O_{7-\delta}$ thin films using microstrip ring resonators technique", Physica C **443**, 9 (2006).
19. C. W. Luo, C. C. Hsieh, Y.-J. Chen, P. T. Shih, M. H. Chen, K. H. Wu, **J. Y. Juang**, J.-Y. Lin, T. M. Uen, and Y. S. Gou, "Spatial dichotomy of quasiparticle dynamics in underdoped thin-film $YBa_2Cu_3O_{7-\delta}$ superconductors", Phys. Rev. B, **74**, 184525 (2006).

20. S. F. Chen, W. J. Chang, C.C. Hsieh, S. J. Liu*, **J. Y. Juang**, K. H. Wu, T. M. Uen, Y. S. Gou, J.Y. Lin, “Anisotropic magnetoresistance of $La_{0.7}Ca_{0.3}MnO_3$ thin film biepitaxial step junctions”, has been accepted by J. Appl. Phys. (2006).
21. T. Y. Cheng, C. W. Lin, L. Chang, C.H. Hsu, J.M. Lee, J.M. Chen, J.-Y. Lin, K. H. Wu, T. M. Uen, Y. S. Gou, **J. Y. Juang**, Phys. Rev. B. **74**, 134428 (2006).
22. Chia-Hung Li , Han-Chi Liu , Shih-Chun Tseng , Yi-Ping Lin , Shih-Pu Chen , Jung-Yu Li , Kwang-Hsiung Wu ,and **Jenh-Yih Juang**,"Enhancement of the field emission properties of low-temperature-growth multi-wall carbon nanotubes by KrF excimer laser irradiation post-treatment" , Diamond & Related Materials 15 (2006) 2010–2014 .
23. W. J. Chang, J.-Y. Lin, T. Y. Chung, J. M. Chen, C.-H. Hsu, S. Y. Hsu, T. M. Uen, K. H. Wu, Y. S. Gou, and **J. Y. Juang**, “Fabrication and X-ray Absorption Spectroscopy in Layered Cobaltate Na_xCoO_2 thin films”, has been accepted by Journal of Magnetism and Magnetic Materials (2006)